creative commons
COMMONS DEED

저작자표시-비영리-변경금지 2.0 대한민국

이용자는 아래의 조건을 따르는 경우에 한하여 자유롭게

- 이 저작물을 복제, 배포, 전송, 전시, 공연 및 방송할 수 있습니다.

다음과 같은 조건을 따라야 합니다:

저작자표시. 귀하는 원저작자를 표시하여야 합니다.

비영리. 귀하는 이 저작물을 영리 목적으로 이용할 수 없습니다.

변경금지. 귀하는 이 저작물을 개작, 변형 또는 가공할 수 없습니다.

- 귀하는, 이 저작물의 재이용이나 배포의 경우, 이 저작물에 적용된 이용허락조건을 명확하게 나타내어야 합니다.
- 저작권자로부터 별도의 허가를 받으면 이러한 조건들은 적용되지 않습니다.

저작권법에 따른 이용자의 권리는 위의 내용에 의하여 영향을 받지 않습니다.

이것은 이용허락규약(Legal Code)을 이해하기 쉽게 요약한 것입니다.

Disclaimer

dCollection

공학박사 학위논문

대규모의 혈관화된 스페로이드 구현이 가능한 3D 프린팅된 메쉬 기반 미세유체 플랫폼

3D Printed Mesh-Microfluidic Platform for Generating Large Scale Vascularized Spheroids

2023년 8월

서울대학교 대학원

기계공학부

이 정 섭

대규모의 혈관화된 스페로이드 구현이 가능한 3D 프린팅된 메쉬 기반 미세유체 플랫폼

3D Printed Mesh-Microfluidic Platform for Generating Large Scale Vascularized Spheroids

지도교수 전 누 리

이 논문을 공학박사 학위논문으로 제출함
2023 년 4 월

서울대학교 대학원
기계공학부
이 정 섭

이정섭의 공학박사 학위논문을 인준함
2023 년 6 월

위 원 장 : 이 호 원 (인)

부위원장 : 전 누 리 (인)

위 원 : 신 용 대 (인)

위 원 : 김 홍 남 (인)

위 원 : 고 지 훈 (인)

Abstract

Organ-on-a-chip is a microfluidic platform for studying complex biological systems by developing biomimetic in vitro models. With the advancements of microfluidic technology, which refers to the manipulation and control of small amounts of fluid at microchannels, precise and dynamic control over cellular microenvironments is enabled. This allows organ-on-a-chip models to become more sophisticated, enabling the implementation of complex in vivo structures and diverse cell culture environments.

Vascularized spheroids or organoids are becoming increasingly important in research to recreate the actual tumor microenvironment. Vascularized models offer a more sophisticated in vivo-like environment, allowing for the utilization of diverse drug toxicity tests through microvessels and studies on flow circulation systems with microfluidics, leading to more advanced results. In vascularized models, important data regarding cultured tissues, tumor or microvessels morphology, and cell-to-cell mechanisms by organ physiology and drug responses can be obtained, allowing for valuable outcomes by tracking and analyzing such data. Thus, organ-on-a-chip have been pivotal in engineering complex in vitro models, such as cancer, infectious diseases, multi-organ system and lymphatic and interstitial flow in the tumor microenvironment, allowing researchers to study disease progression and mechanisms.

However, these platforms have encountered two main limitations. Firstly, the microfluidics-based tumor microenvironment platforms were sufficient for co-culturing small-size tumors, but with the emergence of 3D tissues or organoids, designs that can accommodate larger tissues/explants/spheroids are required. Secondly, as the platforms have advanced, the throughput of experiments has

increased dramatically, but imaging systems have not kept pace. Typically, organ chips implement 3D tumor microenvironments and use confocal microscopes for detailed imaging. However, due to the cost and poor accessibility of confocal microscopes, there is a bottleneck in screening large amounts of imaging data from high-throughput imaging microscopes.

In this thesis, I introduce two new technologies:

Large scale Vascularized Tissue Mesh-Assisted Platform (VT-MAP). VT-MAP is an innovative platform that combines the existing rail-assisted structure with the mesh-assisted structure, enabling the development of large-scale vascularized tissue or organoid models. The platform can provide not only co-cultivation of large-sized single organoids but also enable the cultivation of clusters distributed in various sizes. Additionally, VT-MAP is a platform applicable for drug screening and precision medicine research, providing valuable insights into the drug response evaluation of cells and enabling more accurate and reliable data acquisition. This allows VT-MAP to offer a deeper understanding of the cultivation of vascularized tissues or organoids and drug responses. VT-MAP is expected to overcome the limitations of current in-vitro models and open new possibilities for drug development and precision medicine research by vascularized tissues and organoids.

High-efficiency label-free virtual staining network based on deep learning. Virtual staining provides an effective solution to obtain fluorescent-like images from simple brightfield microscope images without the immuno staining process and relying on traditional microscope equipment. Currently, researchers are exploring methods to achieve virtual staining without the need for conventional cell staining or tissue staining techniques in various fields of biology. Moreover, I have extended the application of virtual staining to label-free live cell imaging. Virtual live cell

imaging represents an innovative approach that allows for the real-time visualization of cellular dynamics without relying on traditional staining techniques. Through the utilization of advanced virtual staining networks and quantitative analysis algorithms, real-time virtual live cell imaging enables the conversion of brightfield images into label-free virtual fluorescence images. This technique provides valuable insights into the behavior and interactions of live cells within their native microenvironment.

I believe that these two technologies have the potential to enhance the field of organ-on-a-chip research in terms of throughput and data analysis. By overcoming the limitations of current platforms, VT-MAP and virtual staining will enable the development of more sophisticated and realistic models of human tissues and organs. This will lead to a better understanding of disease mechanisms and the development of more effective treatments.

Keyword : Organ-on-a-chip, Vascularized tissue, Microfluidics, Large scale, Live cell imaging, Deep learning, Label-free

Student Number : 2017-24396

Table of Contents

List of figures

FIGURE PRESENTS A GRAPH PLOTTING THE FOUR PARAMETERS OF THE ACTUAL BLOOD VESSELS OVER TIME, QUANTIFIED FROM THE VIRTUAL LIVE CELL IMAGES. THESE FOUR PARAMETERS ARE USED TO QUANTITATIVELY MEASURE THE CHARACTERISTICS OF THE BLOOD VESSELS. IT SHOWS THE CHANGES OVER THE COURSE OF 50 HOURS, ALLOWING US TO OBSERVE THE TRENDS FOR EACH PARAMETER.···· 105

Chapter 1. Introduction

1.1. Organ-on-a-Chip

Researchers have utilized various models for cancer and drug development. Until now, animal models (in vivo) and 2D well plate culture (in vitro) models are dominantly used, leading to the accumulation of extensive data. However, these approaches have limitations in adequately mimicking the human body due to constraints in animal experimentation, ethical problems, and inherent differences between humans and animals[1]. To overcome these limitations, there has been growing attention and importance placed on new in-vitro model, called organ chips[2-4], which can replicate the human body's cellular composition and physiological conditions. Organ chips are advanced technologies that mimic realistic human physiological conditions, enabling the evaluation of drug efficacy and the study of complex biological interactions in environments closely resembling the human body[5-8]. Still, fully mimicking the complexity and conditions within the body is difficult[9] (Figure 1.1).

Considering these differences among in vivo, and in vitro, the emergence of organ chips holds significant importance. Organ chips are platforms that implement 3D tissue models outside the body[10], providing an environment similar to conditions within the body and enabling more accurate replication of cellular physiological functions. They offer the advantage of obtaining results closer to in vivo experiments by reproducing the complexity and interactions of tissues outside the body. Organ chips can incorporate crucial biological functions, such as vascularization, allowing for the regulation of factors like blood flow[11, 12], cell-

cell interactions[13], and circulation. Therefore, organ chips provide a model that is more representative of the body compared to in vitro experiments and can yield results comparable to in vivo experiments. This makes organ chips valuable tools in various applications, including drug development and disease mechanism research[14], as they bridge the advantages and limitations of in vivo, and in vitro models.

The use of microfluidics in organ chips has expanded the possibilities for 3D cell culture, including microfluidics systems that allow for greater control over the chemical and mechanical stimuli that cells experience; for example, by controlling the mechanical stress from fluid flow to match the natural flow within vasculature[11]; or, enabling the culture of polarized epithelium at the air-liquid interface[10]; or by matching the stiffness of the culture surface more closely to the stiffness modulus that exists in soft tissue[12]. Despite these advancements, challenges still remain in the development of 3D cell culture systems. These challenges include throughput, customizability, manufacturability, reproducibility, and design modification to meet specific applications. Researchers continue to work on nature materdeveloping new approaches to address these limitations and improve the capabilities of 3D cell culture systems.

	In-vivo 	In-vitro well plate culture 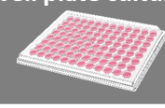	In-vitro Organ chip 
Definition	Experiments using the whole living organisms	Experiments outside of a living organism in a controlled environment	Experiments outside of a living organism in a controlled environment
Advantages	Accurate and lead to near-ideal results	Minimize the use of animals and faster than in-vivo models	Minimize the use of animals and achieve similarity to in-vivo environments
Disadvantages	Time-consuming, Different results from human	Not accurate as the results differ from in-vivo data	Hard to design complex structure, Small-scale culture problem

Figure 1.1. Difference between in-vivo, and in-vitro models

1.2. Requirements for high-throughput vascularized models

Microvessels play a crucial role in the functioning of organs, as most organs exist in conjunction with microvessels[6]. These are responsible for essential functions such as nutrient and oxygen supply, which are vital for cell survival. In vitro models based on 2D well plates, organ or tumor cells are typically cultured in the absence of vasculature, making it challenging to accurately replicate the actual microenvironment[14-18]. Consequently, one of the key roles of organ chips is to implement vascularized models that closely mimic the in vivo environment. By using organ chips to reproduce vascularized tissues, cells can interact within a vascular network and thrive in an appropriate environment. This enables the development of vascularized tissue models that exhibit physiological interactions similar to those observed in real tissues[13, 17, 19-21].

For example, to replicate tubular structures in vitro, vascular endothelial cells can be compartmentalized within a micropillar array, allowing them to self-assemble into a 3D vascular network[22]. Similarly, microgrooves can function as capillary valves[23], enabling co-culture of endothelial cells with astrocytes and pericytes to mimic the blood-brain barrier[24]. Another approach involves using a sacrificial layer of a hollow rod on a 3D hydrogel block to mimic the shape of blood vessels[25]. In neuroscience research, microgrooves and channels within microphysiological systems (MPS) have been utilized to guide complex axons in the central nervous system[26]. Additionally, membrane-embedded models have been employed to simulate layered structures such as alveolar[27], intestinal[28], and placental barriers[29]. By creating a flexible membrane within the MPS, communication between multiple cell layers is facilitated, allowing for a variety of

assays. MPS has also successfully modeled organs with spherical and radial structures, such as the eye, enabling the replication of blinking eyelids and radial angiogenesis. These approaches are driven by a design philosophy rooted in biology[30, 31].

Vascularized models are indeed vital in biology-driven design. The complex network of blood vessels plays a pivotal role to various organs and tissues in the body[17, 22, 32]. Therefore, the development of vascularized models is an ongoing pursuit in the field of organ-on-a-chip (Figure 1.2). These models aim to replicate the physiological relevance and functionality of blood vessels, allowing for the study of complex biological processes in a controlled and realistic environment. Efficient and consistent vascularization techniques are being actively researched to ensure the successful integration of vascular networks within organ-on-a-chip platforms. These techniques involve engineering microfluidic systems that mimic the structural and functional characteristics of blood vessels, enabling the perfusion of nutrients and the maintenance of cellular interactions. Vascularized models have immense potential in drug screening and disease research. They can accurately replicate the microenvironment and pathophysiological conditions of specific organs, facilitating the evaluation of drug efficacy and toxicity[33]. Additionally, these models enable the investigation of disease mechanisms, tissue regeneration, and personalized medicine approaches.

Recently, efforts are underway in various research labs to develop vascularized models, including vascularized spheroids, vascularized brain organoids, and liver models[34], utilizing techniques such as bio printing[35-37]. The goal of these endeavors is to create tissue models that are more realistic and closely resemble the complexity of the human body compared to existing models. Despite these

advancements, there is a continuous increase in the demand for vascularized models that offer high efficiency and reliable results. Therefore, the development and research of more advanced vascularized models that can meet these demands are ongoing.

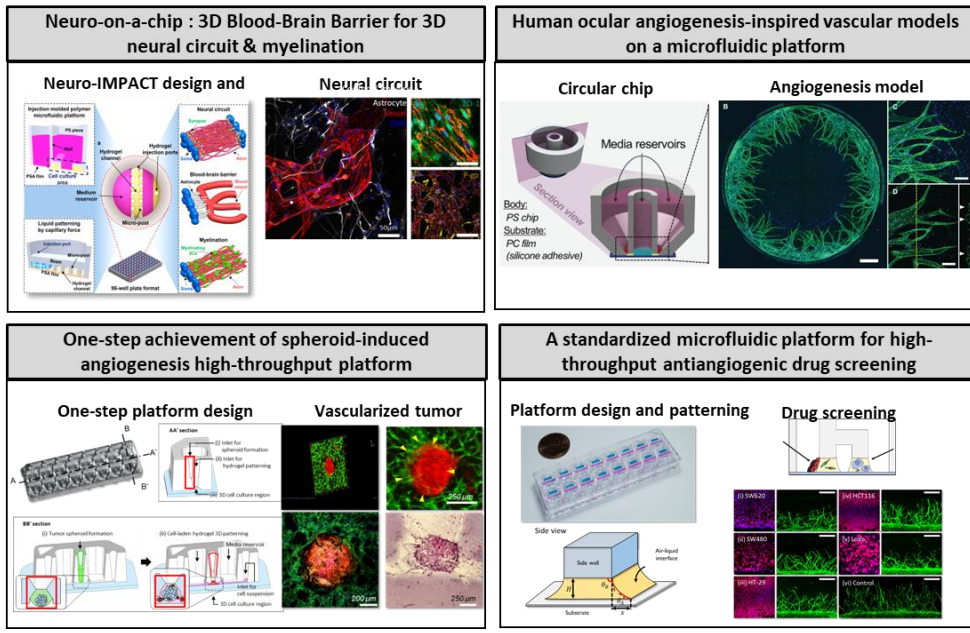

Figure 1.2. Various models of organ on a chip for vascularized models.

1.3. Necessity of large-scale vascularized tissue models

There has been an increasing number of research findings utilizing 3D tissues or organoids similar to in vivo condition[38-40]. In particular, research on organoids has become very active in recent years[27, 41]. Organoids are large tissue structures cultured in vitro that contain functional components of real tissues, as opposed to simple cell aggregates like spheroids. They can be implemented to closely mimic the in vivo tumor microenvironment[15, 42-44] (Figure 1.3). For mimicking in vivo like environment, it is necessary to not only culture organoids but also create a vascularized microenvironment. However, most existing in vitro models have primarily focused on small spheroid-based models[42, 43]. Consequently, there is a lack of models that allow for the co-culturing of large organoids[45] (Figure 1.4). Furthermore, conventional tumor-on-a-chip models typically involve culturing a single spheroid in a well to mimic the tumor microenvironment. However, the tumor microenvironment consists of various clusters distributed in different sizes, making it challenging to replicate by in vitro model.

The emergence of large-scale vascularized tissue or organoid models has opened up new possibilities for studying complex biological processes, regenerative medicine, and drug development. However, current in vitro platforms face challenges in maintaining large-scale vascularization and the functionality of engineered tissues[46, 47]. Vascularization methods such as sacrificial templates or 3D bioprinting[35, 48] have limitations in terms of scalability, reproducibility, and complexity. Additionally, the development of vascularized tissue models that accurately mimic the spatial organization and physiological functions of the human

body's native environment remains a significant challenge. Large-scale vascularized tissue models have great potential in providing insights into disease mechanisms, personalized medicine, and drug screening. Therefore, there is a demand for innovative platforms that support the cultivation of large-scale vascularized tissue or organoids and provide representative models that are more suitable for studying complex biological systems[49].

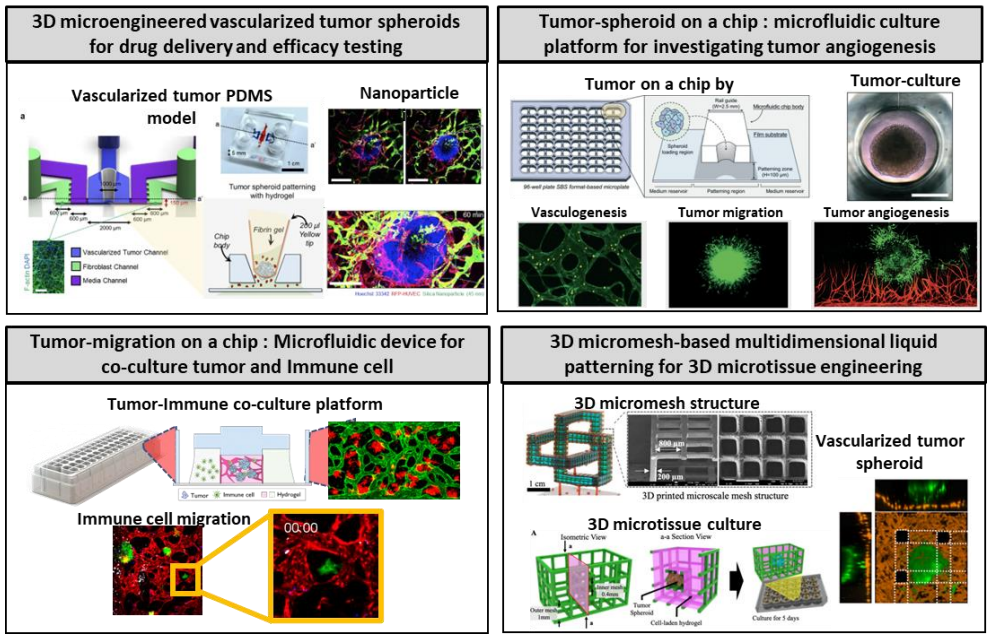

Figure 1.3. Organ on a chip for tumor microenvironment using microfluidics.

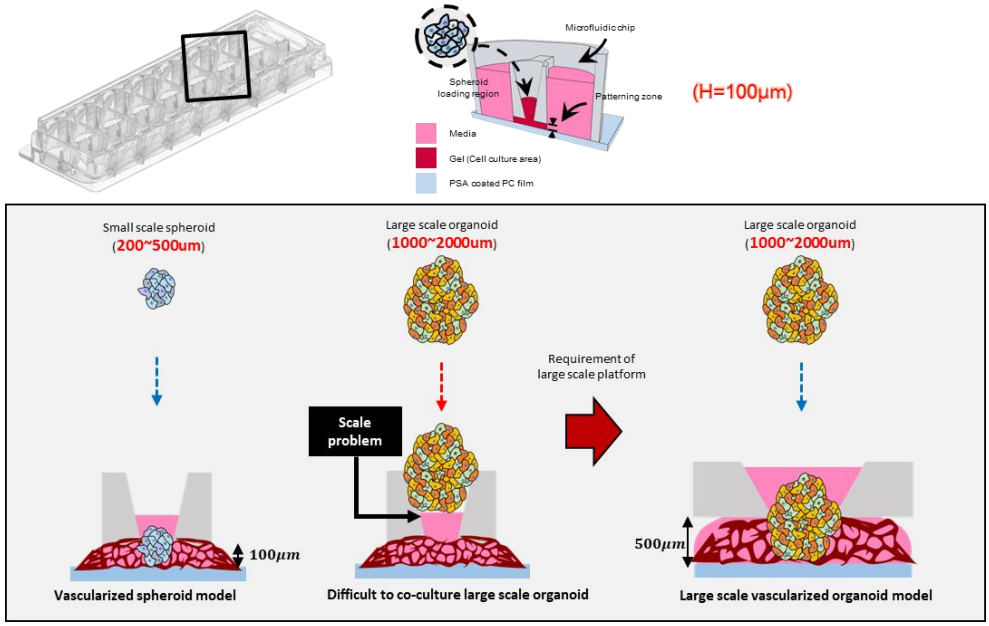

Figure 1.4. Difference between spheroid and organoid culture conditions. Existing vascularized spheroid models are difficult to co-culture organoid. New platform for large-scale vascularized organoid models are required.

1.4. Bottleneck in high-throughput imaging system

In general, confocal microscope is commonly used for imaging in organ chips to reproduce the 3D tumor microenvironment. However, confocal microscope has the drawback of being expensive and slow, although it can provide high-quality images. With the recent advancement of organ chip technology, there has been a significant increase in throughput, leading to bottlenecks in the imaging system. While high-throughput platforms allow for processing multiple samples simultaneously and improve experimental efficiency, the imaging system struggles to keep up with such speed. As a result, there are limitations in capturing a large amount of data within a suitable timeframe[50].

To overcome these bottlenecks, there is a need for rapid and efficient data acquisition methods. Recent advancements in computer vision and deep learning technologies[51-54] have been applied in various biological imaging applications[55-57]. For example, image segmentation is used in cell analysis[58, 59], while image generation is utilized in virtual staining[60] (Figure 1.5). These deep learning techniques enable fast and accurate processing of images that previously relied on manual labor or human intervention. Virtual staining has been used as a technique to generate related results to actual staining, replacing the need for traditional staining methods. Furthermore, Virtual staining technique is incredibly important, especially the ability to obtain virtual-stained images without the need for immuno-staining in live-cell imaging, represents an innovative advancement. Previously, immuno-staining caused damage to cells and limited imaging to specific end points, making it challenging to observe data throughout the entire process. However, with the use of virtual staining, it is now possible to capture

subtle changes and detailed information that was not previously visible, by examining data throughout the entire process (Figure 1.6). Moreover, the label-free nature of virtual staining allows for long-term cell culture without any damage to cells, resulting in higher reliability of the acquired data.

Therefore, introducing innovative technologies such as deep learning-based virtual staining can provide a solution to overcome these bottlenecks and establish a system capable of generating high-quality images without relying on confocal microscope. By utilizing such technologies, efficiency in imaging workflows can be improved, bottlenecks can be addressed, and accurate and rapid data acquisition becomes possible. Thus, the integration of these advanced techniques can enhance the performance of the imaging system, allowing it to keep up with the increased throughput in organ chip technology.

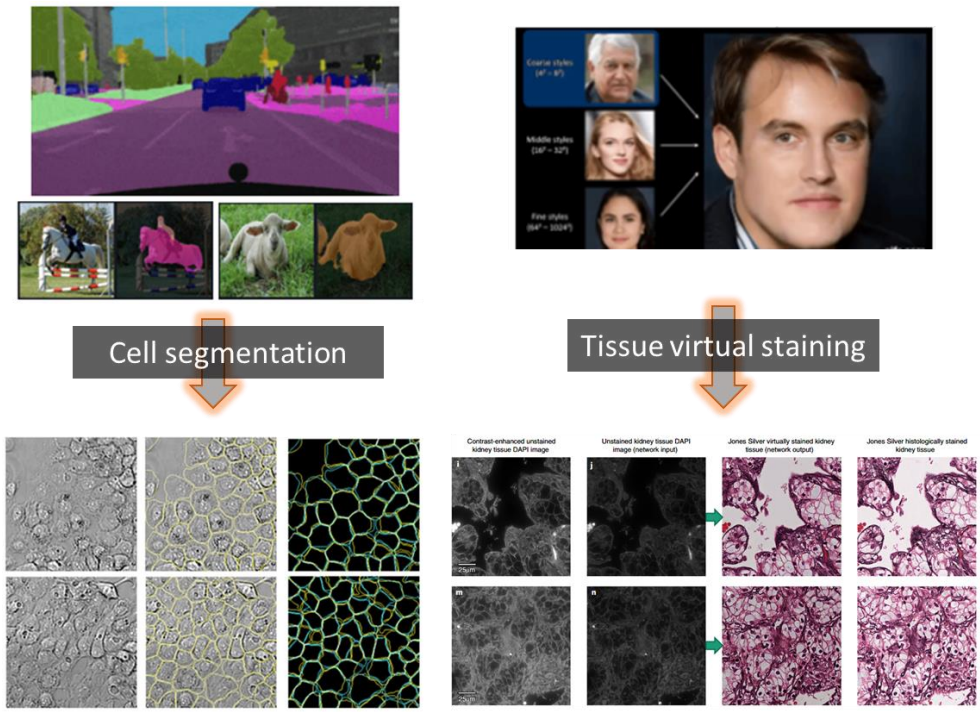

Figure 1.5. Advancements in computer vision technology with deep learning for biology field.

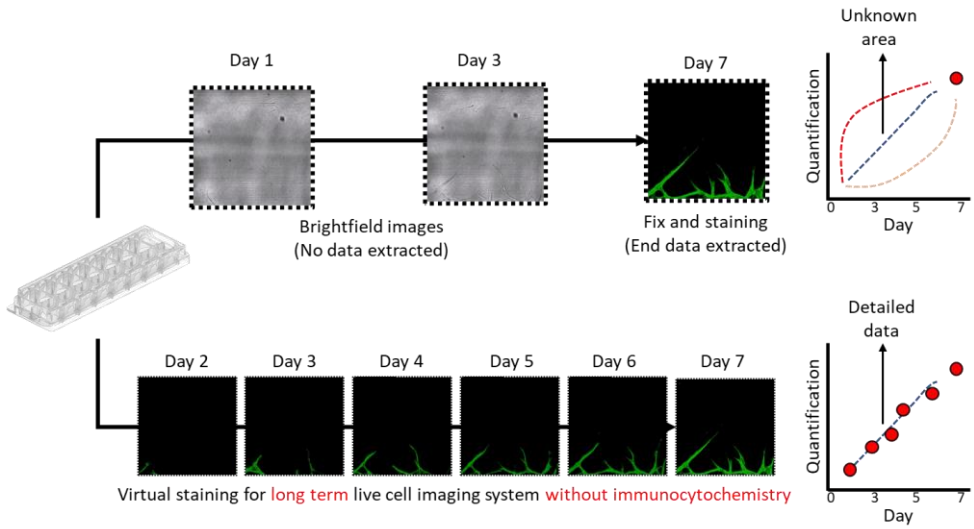

Figure 1.6. Importance of label-free live cell imaging via deep learning. Label-free live cell imaging allows for the observation of subtle changes and detailed information throughout the entire process, unlike the previous approach that only captured data at the endpoint. Furthermore, being label-free, it enables long-term culture of cells without causing any damage, enhancing the reliability of the data obtained.

1.5. Purpose of research

The developed in vitro models thus far have played a significant role in recapitulating the tumor microenvironment and have successfully yielded various drug testing and in vivo-like results. These models have been successful in developing high-throughput tumor microenvironment models by transitioning from PDMS to Polystyrene (PS) and utilizing injection molding. They have demonstrated high reproducibility within the platform through microfluidic analysis, enabling the implementation of vascularized tumor environments that closely resemble in vivo conditions. However, these platforms were primarily designed for small spheroids and were not suitable for co-culturing large-scale organoids. Furthermore, with the advancement of high-throughput platforms, difficulties have arisen in capturing and processing all the data using existing imaging systems. Therefore, there is a need for a new spheroid chip on the hardware side and a need for technology to address the bottleneck of existing imaging systems on the software side.

In this thesis, we propose a new platform that allows for co-culturing of large-scale organoids along with vasculature. This platform not only enables co-culturing of large organoids but also accommodates multi-cluster organoids that mimic in vivo-like environments. Additionally, an algorithm for precise data extraction has been developed. Furthermore, to address the bottleneck of imaging systems, we introduce virtual staining technology to the field of organ-on-chip. By applying deep learning-based virtual staining, fluorescent images can be obtained from simple brightfield images without the need for a confocal microscope. Moreover, by applying this technology in real-time, we can track the morphological changes of vasculature and tumors within the organ-on-chip, thereby obtaining previously unobserved data.

Chapter 2. Large-Scale Vascularized Tissue Mesh-Assisted Platform (VT-MAP): A Comprehensive Approach for Mimicking Tumor Microenvironment and Analyzing Cluster Viability

2.1. Introduction

Until now, there has been rapid progress in understanding the pathological characteristics of cancer[61] and the importance of the tumor microenvironment[62]. Consequently, there is a growing need for reliable experimental models in cancer therapy development and tumor biology research[63-67]. Particularly, with the discrepancies between animal experimental results and clinical outcomes and the ethical concerns surrounding animal experiments, the importance of in-vitro models utilizing human cells has become even more pronounced[1]. In-vitro models have been developed to reflect the complexity of the tumor microenvironment[65] and provide valuable information for drug screening and tumor biology research.

Recently, platforms simulating complex structures such as 3D tissue models and vascularized tissue models have emerged. These platforms are recognized as crucial tools for reproducing in-vivo like conditions of tumor microenvironment and investigating various biological processes associated with cancer development and progression[15, 17, 42, 49, 68]. Furthermore, these platforms play an important role in the development of cancer therapeutics and personalized treatment strategies[69-71]. However, the emergence of large-scale

tissues and organoids poses challenges for the study of vascularized tissue or organoid models[72-74]. Previous platforms were effective at small scales[43, 75], but culturing large-scale tissues or incorporating clusters of diverse sizes and shapes proved challenging. These limitations constrain the ability to accurately reflect the complexity of the realistic tumor microenvironment and may affect the reliability and reproducibility of research outcomes.

The need for in-vivo like and accurate mimicking of the tumor microenvironment in large scale vascularized tissue or organoid models has become increasingly important[49, 76]. However, current in-vitro models often fail to sufficiently replicate the large scale of the tumor microenvironment, highlighting the demand for more advanced models. The combination of 3D vascularized tumor models and mesh-assisted structure has emerged as a promising approach for large scale tumor microenvironment. Here, I present a large-scale vascularized tissue mesh-assisted platform called VT-MAP. VT-MAP overcomes the limitations of the previous rail-assisted approach and provides an effective platform for the cultivation of large-scale tissues, including vascularized tissues or organoids. By incorporating fluid dynamics analysis and a novel algorithm, VT-MAP enables the extraction of diverse information related to the size, growth rate, and viability of vascularized tissues.

2.2. Material and method

2.2.1. Device fabrication

The device was designed using Solidworks (Dassault Systems) and fabricated with 3D printer, Figure 4 Standalone (3D systems). After printing, the device was washed with isopropanol and cured with ultraviolet light in 380nm for 1 hour. The device was dried and single-sided PSA (Pressure sensitive adhesive) film (IS-00820, IS solution) was attached at the bottom side of device to obtain space for hydrogel patterning. Then, the device was sterilized with UV in a bio-hazard safe bench while cell preparation for experiment. O2 plasma (Femto Science) was treated for 3 minutes in 75W, 50kHz to make the device hydrophilic before hydrogel patterning in device.

2.2.2. Cell culture

Human umbilical vein endothelial cells (HUVECs, Lonza) and lung fibroblasts (LFs, Lonza) were cultured in endothelial growth medium-2 (EGM-2, Lonza) and fibroblast growth medium-2 (FGM-2, Lonza) respectively to reconstruct 3D vascular network surrounding organoids. All cells were cultured in a humidified incubator at 37℃ and 5% CO2.

2.2.3 3D vascular network formation and reconstruction of tumor organoid microenvironment

For reconstruction of tumor organoid microenvironment, difference of cell proliferation speed between cancer cells and other cells related to vascular network formation (HUVECs and LFs). On day 0, HUVECs and LFs were firstly prepared to develop 3D vascular network surrounding tumor organoid in outer area. HUVECs

and LFs were mixed with 2.5mg/mL of fibrinogen hydrogel (Sigma Aldrich) with a number ratio of 2:1 at a cell density of 4X106 cells/mL and 2X106 cells/mL as final concentration, respectively. On day 2, medium in inner area was sucked out and mixture of tumor organoids, HUVECs, LFs and hydrogel was filled inner area. Tumor organoids were dissociated as a single cell in 2X106 cells/mL as the final concentration and HUVECs and LFs were in same final concentration with 3D vascular network formation. The device was maintained in the incubator for whole experiment.

2.2.4. Drug treatment

For the observation of drug performance in the device, drugs were treated on the vascularized tumor organoid microenvironment in the device. The following chemotherapeutics were used: 5-Fluorouracil (5-FU, R&D Systems), Irinotecan (CPT11, R&D Systems), and Oxaliplatin (R&D Systems). Irinotecan and oxaliplatin were treated as the monotherapy or combination treatment with 5-FU. Control groups were treated with fresh EGM-2 and irinotecan and oxaliplatin were diluted in 200mM in EGM-2 for monotherapy. 50mM, 100mM, and 200mM of 5-FU were mixed in equal concentrations of irinotecan or oxaliplatin for combination treatment, respectively. The drug treatment was sustained for 24 hours in incubator to observe the drug performance.

2.2.5. Live/Dead assay

Alexa Fluor 488-tagged variants of anti-epithelial cell adhesion molecule (EpCAM, BioLegend) and propidium iodide (PI, Sigma Aldrich) were used to detect dead signal by drug treatment from tumor organoid microenvironment. Cells were stained using EGM-2 in the proportion 200:1 and 1000:1 for EpCAM and PI,

respectively. EpCAM was added in the mixture of drug and cell culture medium while drug treatment. After 24 hours, the cells were washed with EGM-2 mixed with PI and imaged by confocal microscope (Nikon Ti 2) after 30 minutes. We calculated dead signal ratio by (the fluorescence intensity of dead cells overlapped with EpCAM signal)/(the fluorescence intensity of tumor organoid cells with EpCAM signal).

2.2.6. Quantitative image analysis

Image acquisition was conducted by confocal microscope (Nikon Ti-2) and imaging software (NIS-Elements). To quantify the viability and area of organoids, the confocal images were projected by Z-axis with max intensity method. As organoid images had various morphology and contrast, pre-process with histogram equalization and normalization was applied for detecting their contour line by Python 3.7 and OpenCV package. Within the contour line, green signal pixels with EpCAM staining for entire area of one organoid and red signal pixels with PI staining for dead area of the organoid were calculated for quantifying the size and viability. We quantified pixel area data in terms of size and viability of the organoid in different drug conditions using Prism (GraphPad).

2.3. Result

2.3.1. Combination of rail-assisted strucutre with mesh-assisted structure for capturing large height microfluidic injection

In the context of organ chips, the rail-assisted microfluidic patterning method is widely employed, which leverages the spontaneous capillary force (SCF). This technique involves patterning microfluidic channels through small gaps, a process that offers both rapid execution and high success rates, thereby facilitating a stable environment. Analyzed from a fluid dynamics perspective, SCF takes advantage of Laplace pressure, which is found to have a linear relationship with the height of the rail channel. In practical terms, a stable environment suitable for patterning is maintained when the channel height is 100um. However, when the channel height increases to 500um, it transitions into a region of patterning failure, making it difficult to anticipate successful patterning (Figure 2.1A).

As the channel height increases to 500um, the condition shifts to $Pw < Pr$, which disrupts the intended operation of the SCF. Furthermore, as the channel height increases, the rail-assisted microfluidic patterning fails to function properly. Especially for SCF with a low contact angle, the fluid spreads along the bottom film before even filling a height of 500um (Figure 2.1B), which exacerbates this issue. However, to overcome this problem, we introduce a mesh-assisted structure. This mesh structure assists by enabling the fluid to fully cover areas with high gaps and effectively controls the fluid spreading laterally (Figure 2.1C).

By combining rail and mesh structures, we have successfully developed a platform capable of culturing large-scale vascularized tissues or organoids, an

achievement that was challenging with previous methodologies. Notably, the mesh structure provides greater design flexibility than the rail structure, enabling the creation of complex structures that were difficult to achieve with rails alone. This proves particularly beneficial in implementing complex structure and replicating intricate tumor microenvironments.

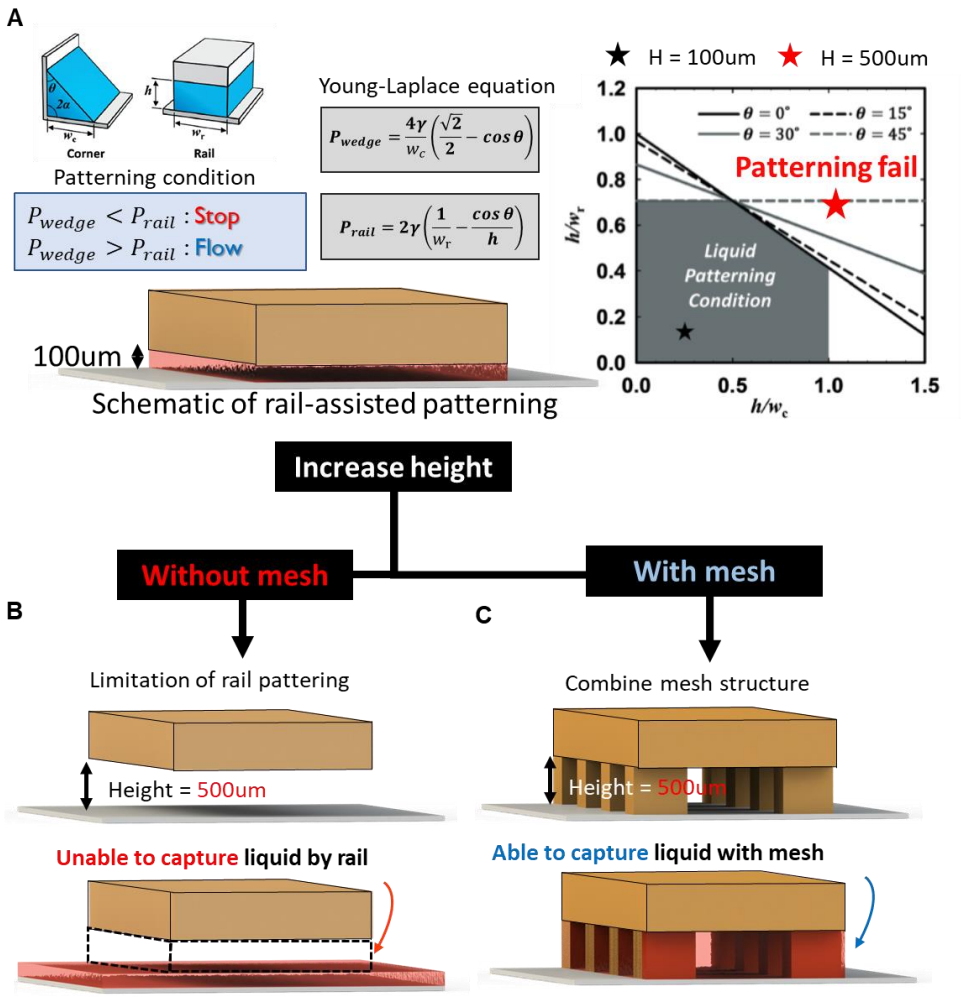

Figure 2.1. Microfluidic patterning principle of rail-assisted structure. (A) Spontaneous capillary force by Young-Laplace equation were utilized for efficient and successful channel patterning in organ chips. But the gap of channel is limitation of small scale. According to the equations of wedge and rail, the formulations are only valid at small gaps, and as the gap expands, patterning becomes increasingly challenging. Particularly, when scaling up to a larger dimension, increasing the gap fivefold which is suitable for large scale vascularized tissue model, the failure condition for patterning becomes clearly apparent, as denoted by the red dots on the graph. (B) Combination of mesh-assisted structure for supplement large scale

platform. When the gap increases fivefold, the fluid disperses along the bottom film before it can pattern along the rail, preventing proper patterning (C). To resolve this issue, the introduction of a mesh-assisted structure can be observed. The mesh structure serves to prevent the spread of the fluid, facilitating correct patterning.

2.3.2. The development of Vascularized Tissue – Mesh Assisted Platform (VT-MAP)

VT-MAP is a platform that mimics the development process of vascularized tumors. In the process of tumor formation in the body, cancer cells first metastasize through fully developed blood vessels. Metastatic cancer cells establish themselves around the blood vessels and recruit nearby blood vessels to supply nutrients, gradually growing. Ultimately, they can be depicted as structures surrounded by blood vessels (Figure 2.2A). The process to simulate this environment in organ chip is shown in Figure 2.2B. To culture large-scale tissues in the previous rail-assisted chip, the system had to scaled up and the height was increased. A mesh-assisted structure was added to pattern the fluid. Finally, the structure was completed by creating holes in the middle to accommodate the spheroid, simulating the structure surrounded by blood vessels. This represents the closest possible replication of the morphological microenvironment of a vascularized tumor.

The overall chip structure of the VT-MAP can be seen in Figure 2.3A. This platform consists of a mesh-formed rail structure (both mesh width and height are 500um), which curves around the center. This curved rail structure serves as the area for forming the vascular network. The open circular region surrounded by the rail (diameter 1500um) is the space for loading the vascularized organoids. The output width of the end of this circular region is designed to be 800um, preventing organoids larger than 1000um from exiting (Figure 2.3A). This open design is intended to allow easy injection of various sizes of organoids without size limitations.

The mesh attached to the rail is located only on the perimeter, with the interior being a simple open structure (Figure 2.3B and Figure 2.3C). The externally

placed mesh prevents fluid from spreading along the bottom film, and the internal open structure maximizes the interactive area between the vessels and organoids. This design benefits vascularized tissues in drug response or medium delivery.

The VT-MAP undergoes a two-step patterning process (Figure 2.3B and Figure 2.3C). The first step is to pattern the vascular area with the primary goal of forming a vascular network. This process forms a pattern that neatly encapsulates the organoid area by injecting into the vascular area through a rectangular injection port. At this time, it can be confirmed from the cross-sectional view that a mesh structure is located on the outer edge of the vascular area, while the interior is an open structure (Figure 2.3D).

The second step is the injection process into the organoid area. The organoid area created by patterning the vascular area is naturally open but is seen to be encapsulated by the vascular area. During injection, patterning occurs only in the organoid area. This two-step process enables the injection of large-scale tissues between vessels. In this way, the configured VT-MAP provides an effective platform for implementing complex biological models.

Figure 2.4A shows the success of patterning depending on the presence or absence of a mesh structure and the contact angle in a 500um gap. The results indicate that more stable patterns are formed when the contact angle is low (that is, when the fluid adheres better to the surface) and when a mesh structure is present. This demonstrates that the mesh structure stabilizes the movement of the fluid and that the lower the contact angle, the better the fluid adheres to the surface, making it easier to form a pattern. Figure 2.4B presents a series of images that demonstrate how the first patterning process progresses over time. You can observe how the

vascular area fills and patterns over time. This process provides insight into how VT-MAP technology achieves high-precision patterning.

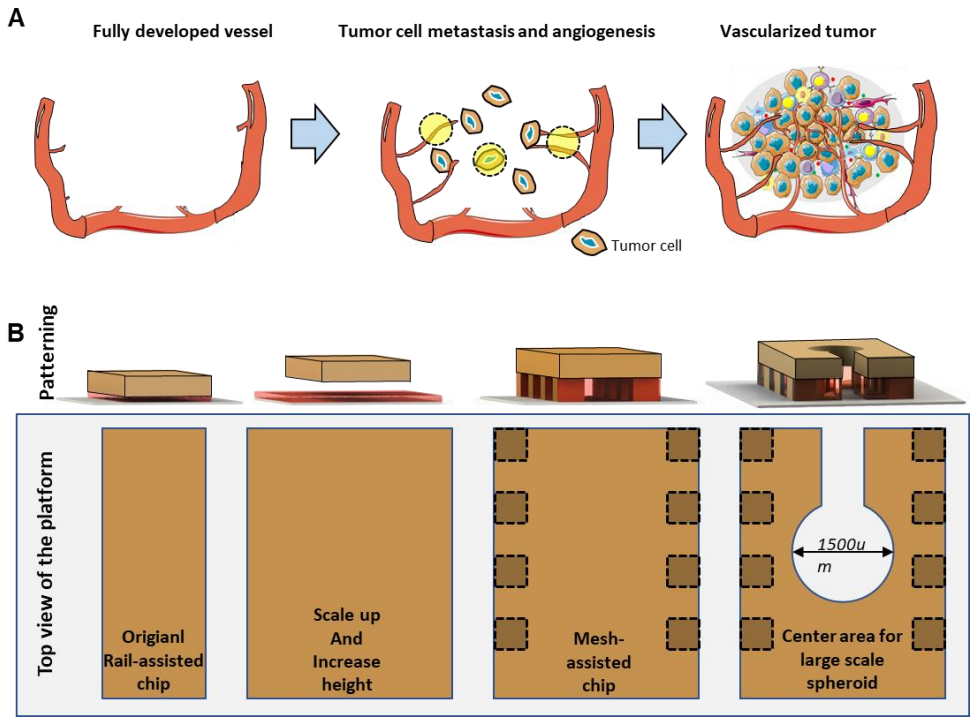

Figure 2.2. Mimic in-vivo tumor microenvironment of vascularized tumor. (A) Process of cancer metastasis via blood vessel. Cancer spreads through blood vessels, and some cancer cells escape through the vessels and migrate to nearby areas. They start absorbing nutrients from surrounding blood vessels and gradually develop. (B) Mimic the vascularized tumor morphology by organ chip by separating section and surrounded structure with mesh-assisted platform.

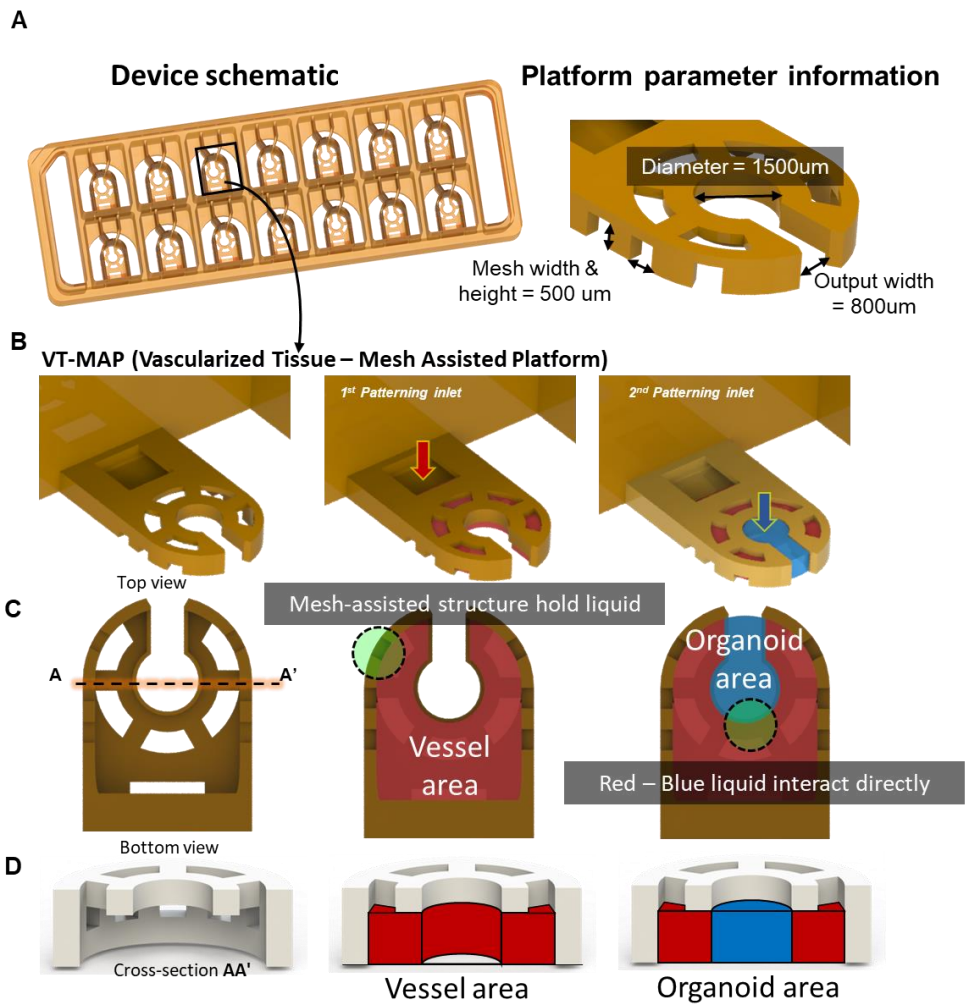

Figure 2.3. Device schematic of VT-MAP and patterning process. (A) The VT-MAP is designed as a chip the size of a standard slide glass, with the sizes of various structures inside it precisely determined. As shown in the figure, the diameter of the inner region is designed to be 1500um to effectively co-culture organoids. In addition, to prevent organoids from leaving the chip, the output width is set to 800um. The width and height of the mesh structure are also determined to be 500um each. (B), (C), (D) The patterning process of the VT-MAP proceeds in two steps. The first step is filling the vascular area with the aim of forming a vascular network. The presence of a mesh structure prevents the fluid from spreading in other directions and allows

patterning to occur only in the desired area. In this step, the vascular area is marked in red. The second step is filling the organoid area, with the goal of injecting large-scale organoids. In this step, the organoid area is marked in blue and interacts directly with the vascular area. Through these two steps, effective patterning and co-culture are possible, enabling the study and modeling of complex biological systems.

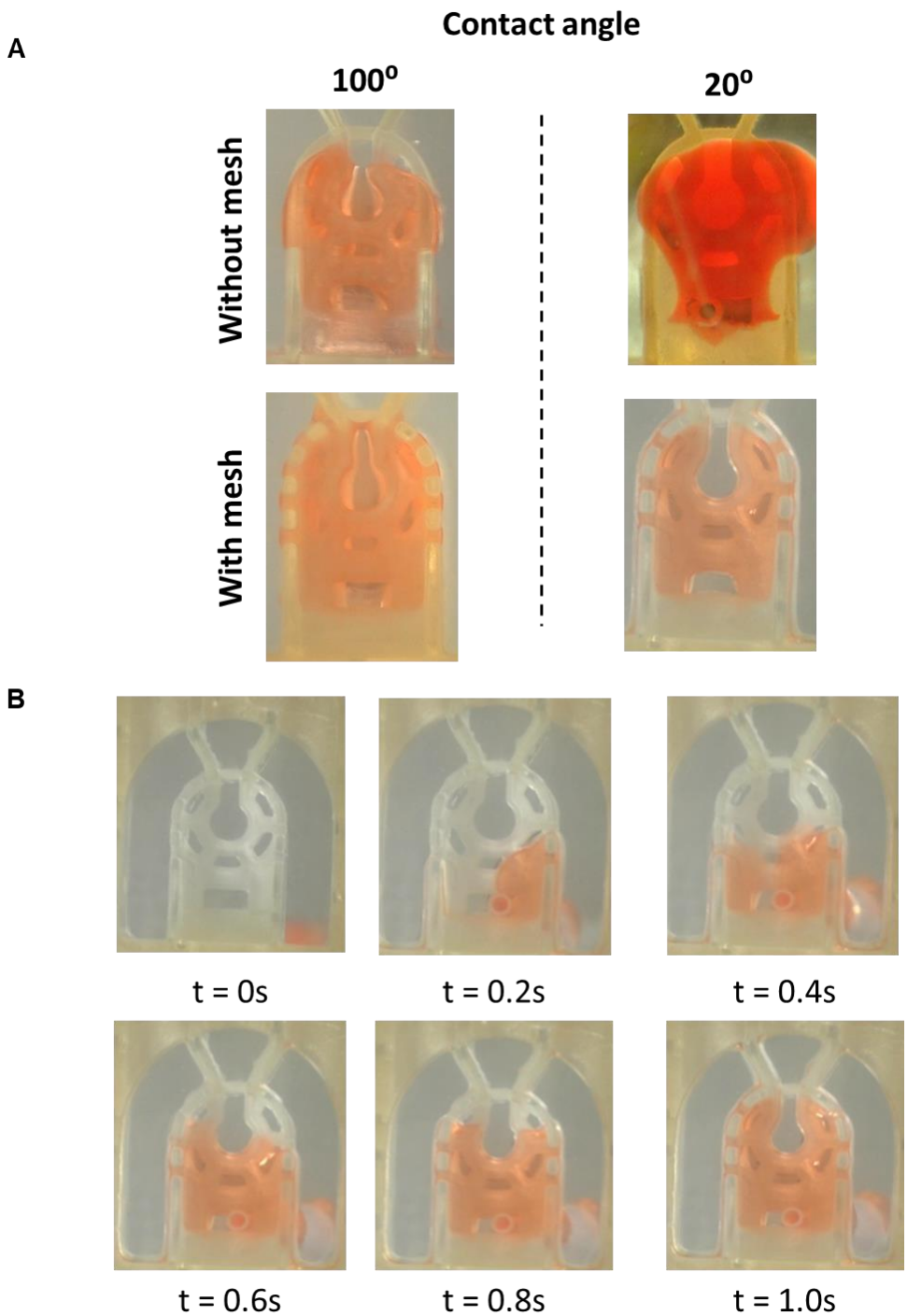

Figure 2.4. The role of micro mesh structure and contact angle condition. (A) The success of patterning based on the presence or absence of a mesh structure and contact angle when the gap is 500um. Stable patterns are only demonstrated when

the contact angle is low and a mesh is present. (B) This image illustrates the first patterning process over time (for 1 second).

2.3.3. Microfluidic analysis approach of VT-MAP

The Young-Laplace pressure is essential for understanding and explaining the movement of fluids and is a valuable tool for controlling fluid patterning (Eqs. 1). In conventional rail-assisted platforms, this principle is utilized to design the fluid to form patterns along the rails in a specific direction. However, VT-MAP introduces a mesh structure, deviating from the conventional design, to prevent the fluid from bursting into the central organoid area while maintaining a circular pattern. To achieve this, two pressures, namely the Forward Laplace Pressure (FLP) and the Burst Laplace Pressure (BLP), are compared. Figure 2.5A illustrates how FLP and BLP act during the pattern formation process, represented by the red regions. The diameter of the vascular area is denoted as R2, and the diameter of the organoid area is denoted as R1. By utilizing the principles of Young-Laplace pressure in this manner, more precise control over the desired pattern formation becomes possible.

$$\Delta P = \gamma \left(\frac{dA_{LG}}{dV} - \cos\theta \frac{dA_{SL}}{dV} \right) \qquad \textbf{Equation 1}$$

FLP represents the formation of a circular pattern along the Mesh-assisted structure, preventing the fluid from bursting into the central area. This can be expressed mathematically by defining theta as the degree to which the fluid rotates in a circular manner around the origin and w1 as the length of the forward face when FLP occurs. Additionally, the delta variable is used to represent changes over a short period of time. In this setup, each red point can be transformed into an orthogonal coordinate system composed of R_1 and θ. Utilizing this, we can obtain the following equation (Eqs. 2), allowing us to understand the relationship between the rate of change in FLP and the various variables. By employing these equations, we can gain a more precise understanding and control of circular pattern formation in

VT-MAP. If BLP is smaller than the FLP value, the fluid is pushed toward the central area due to the Young-Laplace pressure toward the organoid region, preventing the formation of a circular pattern and hindering the desired patterning. In this case, the fluid tends to move toward the central area rather than spreading in a circular manner, and this can be expressed mathematically as an equation involving R_1 and θ (Eqs. 3).

$$\Delta P_{forward} = \gamma\left(\frac{\sin\theta + 1}{\sin\theta\,(R_2 - R_1\theta\sin\theta)} - \frac{2\cos\theta^*}{h}\right) \qquad \textbf{Equation 2}$$

$$\Delta P_{burst} = \gamma\left(\frac{2}{R_1\theta} - \frac{2\cos\theta^*}{h}\right) \qquad \textbf{Equation 3}$$

In order for the fluid to pattern in the desired manner, the Forward Young-Laplace pressure must always be smaller than the Burst pressure (Eqs. 4). Figure 2.5B represents the conditions that satisfy this criterion as a graph with respect to θ.The positive region in the graph represents successful conditions where stable patterning occurs along the circular path, while the negative region represents failure conditions where the fluid bursts towards the center instead of following the circular pattern. The graph depicts the conditions for R_1 values of 0.5, 0.7, 1.0, 1.2, and 1.5. In VT-MAP, the actual R_1 value used is 0.75, and the results from the image on the right confirm the successful formation of the pattern. Conversely, for R_1 values of 0.9 and 1.2, the pattern formation is observed to be almost failed.

$$\boldsymbol{\Delta P_{forward} < \Delta P_{burst}} \qquad \textbf{Equation 4}$$

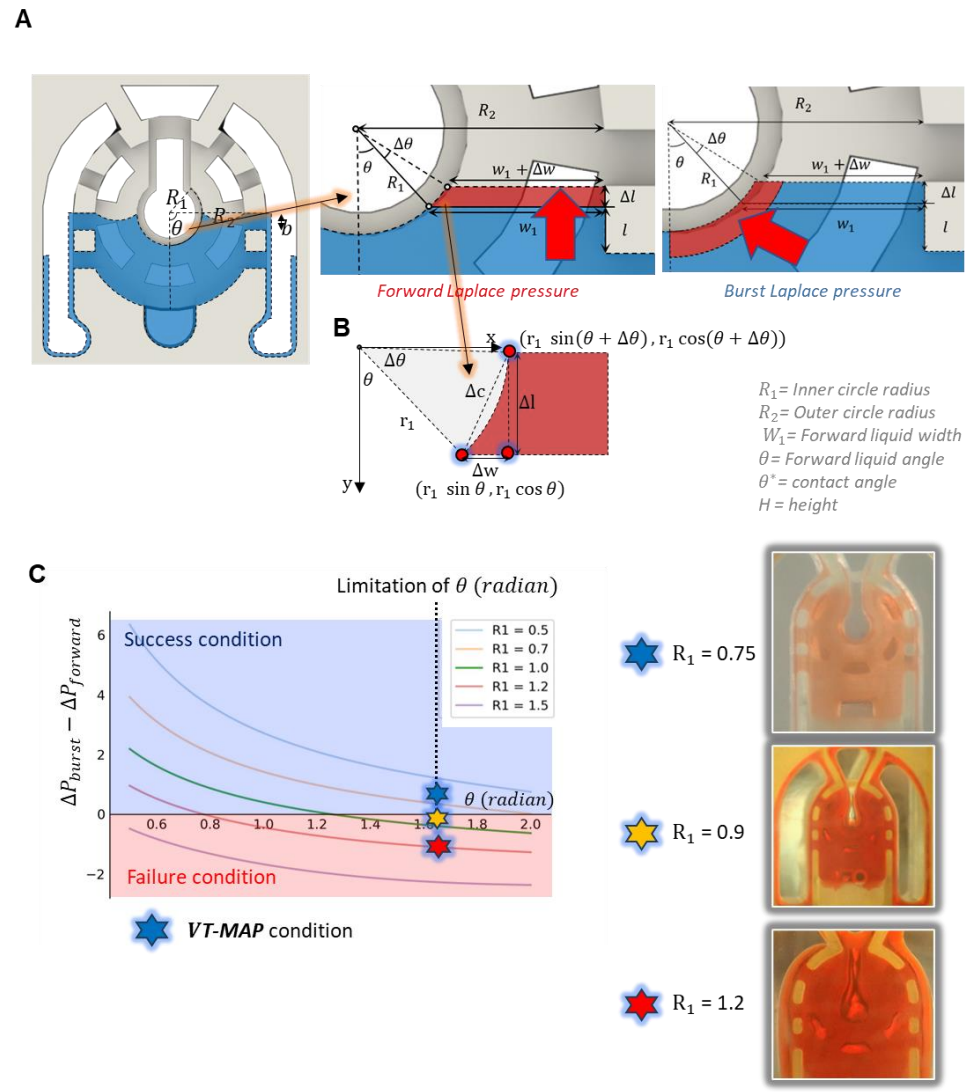

Figure 2.5. Patterning principle of VT-MAP. (A) Laplace pressure of forward condition and burst Laplace pressure condition. (B) Success and failure condition of $\Delta \boldsymbol{P_{burst}} - \Delta \boldsymbol{P_{forward}}$ and specific condition of three $\boldsymbol{R_1}$ **and** $\boldsymbol{\theta}$. $\boldsymbol{R_1 = 0.75}$, $\boldsymbol{R_1 = 0.9}$ **and** $\boldsymbol{R_1 = 1.2}$ show in figure. 0.75 is the design condition for VT-MAP that demonstrates successful patterning. On the other hand, 0.9 and 1.2 exhibit unstable patterning as they deviate from the success condition.

2.3.4. Tumor microenvironment with vascularized organoid on VT-MAP

To assess vascularization on the vascularized tissue platform, we conducted pre-experiments. In the vascular region, HUVECs and LF were injected at a final concentration of 4 million cells per ml and 2 million cells per ml, respectively. Fibrin gel was mixed with the cells for scaffold formation. Two vascularization phenomena, Angiogenesis and Vasculogenesis, were investigated during these experiments. For Angiogenesis experiments, LF and fibrin extracellular matrix were introduced into the vascular region, while HUVECs were attached in the organoid region. This setup allowed us to observe the process of vascular development and the interactions between the two regions. In Vasculogenesis experiments, both HUVECs and LF, along with fibrin extracellular matrix, were injected into both the vascular and organoid regions to observe the connection and formation of blood vessels between the two regions (Figure 2.6A). Lastly, to verify perfusion, red microbeads with a diameter of 4.0 μm were used. These microbeads were flowed through the vascular region and observed to reach the organoid region via the vascular channels, demonstrating a stable drug delivery model (Figure 2.6B). These experiments confirmed that the designed platform could successfully reproduce vascularized tissues and ensure stability in drug delivery.

For large-scale vascularized tissue model, spheroids with a diameter of 1000 μm or larger were prepared in a U-shaped 96-well plate and cultured for 3 days. The platform surface was treated with O2 plasma to facilitate cell attachment. On day 0, HUVECs and LF, along with fibrin extracellular matrix, were injected into the vascular region, while the remaining regions were filled with EGM-2 media. The

cultures were allowed to develop for 2 days. Afterward, the EGM-2 media in the organoid region was removed, and previously cultured spheroids were injected into the region along with HUVECs and LF embedded in fibrin extracellular matrix (Figure 2.7A). The samples were then fixed and subjected to imaging for 3 days. Figure 2.7B demonstrates the formation of a tumor microenvironment, where the spheroids are surrounded by well-developed blood vessels. In contrast to previous organ chips, this approach successfully achieved the implementation of large-scale vascularized spheroids with robust vascularization in the surrounding area.

Moreover, the co-culture method of vascularized multi-cluster organoids, as shown in Figure 2.7C, is depicted. This approach differs from the previous method in that it involves culturing organoid clusters of various sizes within the organoid region, allowing them to grow at different rates. Diverse data, such as relationship between growth rates and drug responses, can be obtained based on the varied characteristics of organoids within a single sample. Figure 2.7D demonstrates the injection of fragmented larger spheroids into the organoid region. This results in the distribution of organoid clusters of different sizes within a single region.

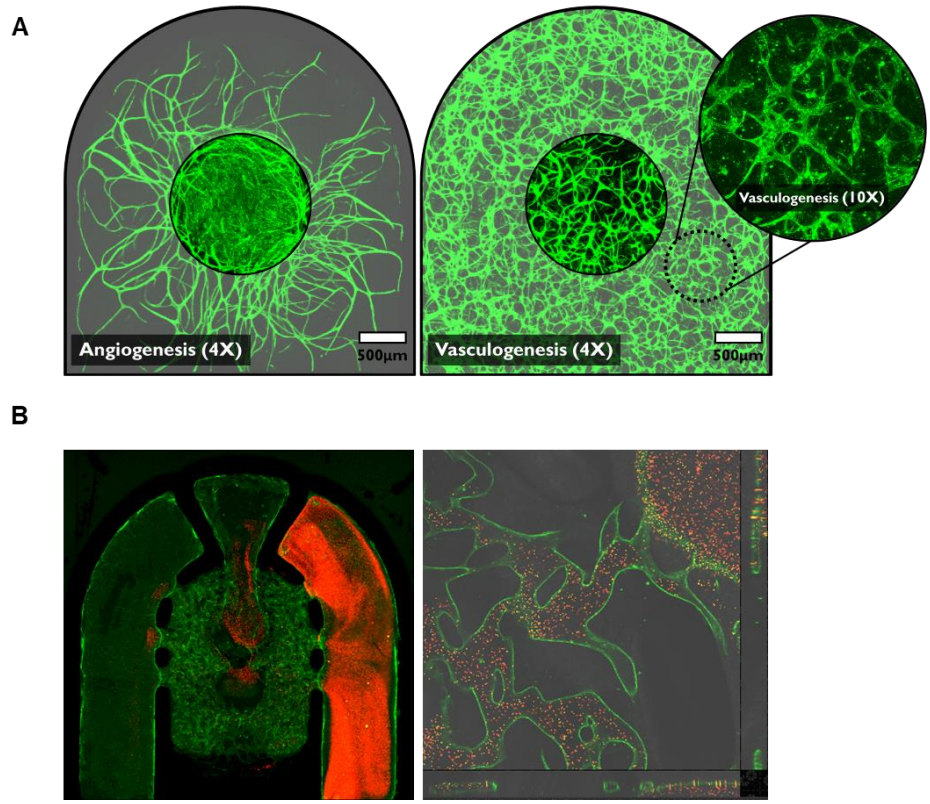

Figure 2.6. Angiogenesis and vasculogenesis application and perfusable test on the platform. (A) This image shows the vascularization test conducted on VT-MAP, demonstrating the implementation of angiogenesis and vasculogenesis. The Vascular area and the Organoid area of VT-MAP interact with each other. (B) To verify the vascularized vessels, red microbeads (diameter 4μm) were introduced into the blood vessels. The microbeads flow through the vessels from the media channel to the inner area, demonstrating their distribution within the blood vessels.

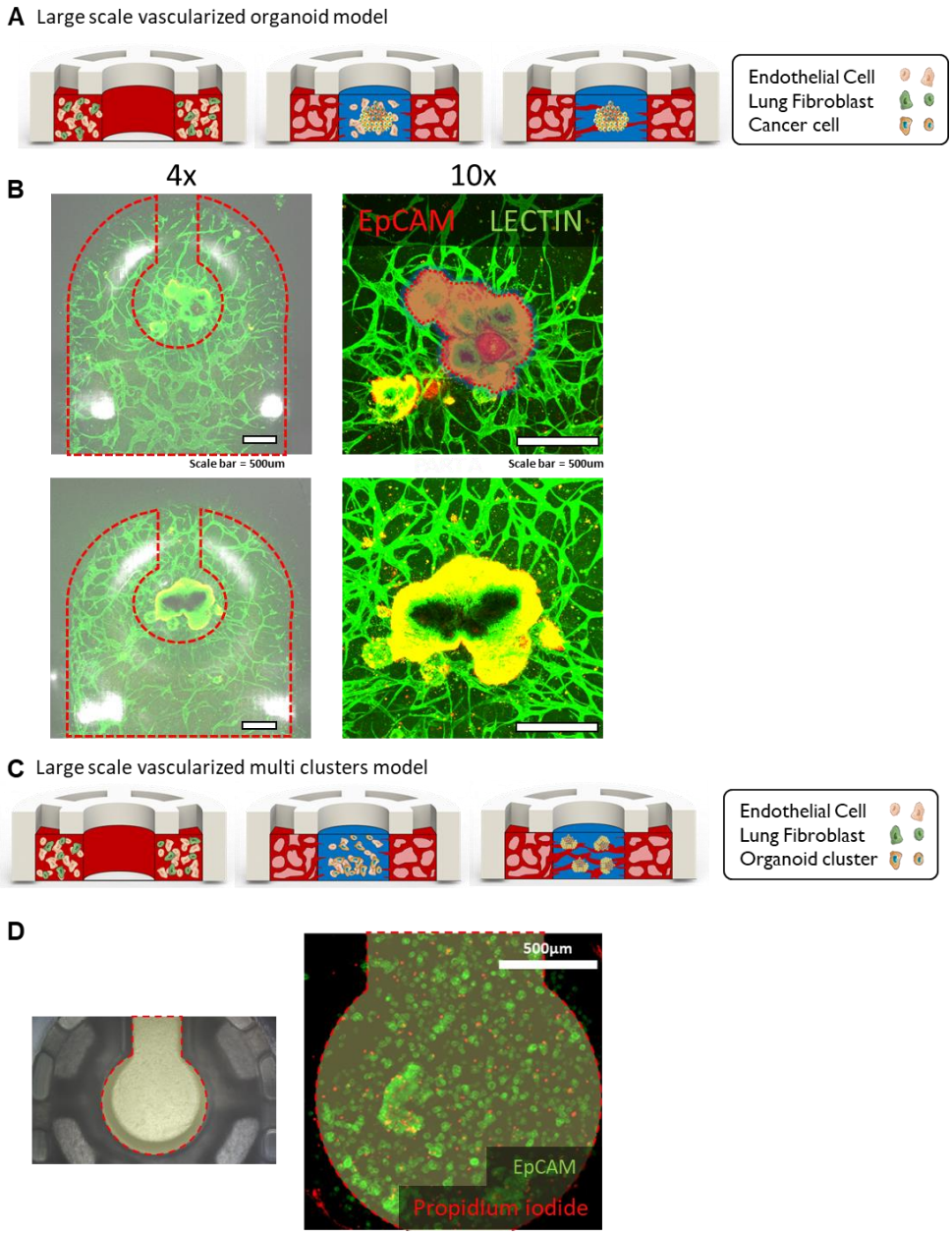

Figure 2.7. Tumor microenvironment on the platform. (A) This figure represents the overall process of co-culture large-scale vascularized organoids in VT-MAP. (B) The vascularization of spheroids with a diameter larger than 1000μm on the platform are introduced. Green signal is micro vessel signal by Lectin and red signal is tumor signal by EpCAM staining. (C) Illustration depicting the process of co-culturing

clusters of various sizes. (D) Result of culturing organoid clusters of different sizes within a single well on the platform.

2.3.5. Novel high-throughput algorithm for multiple organoids and quantitative analysis

Colorectal tumor organoids were dissociated as single cells and loaded in the device to form vascularized microenvironment. Single tumor organoid cells formed various size of clusters in hydrogel(Figure 2.8A). The individual viability of clusters can vary depending on their size. The conventional analysis method, such as a live-dead assay, measures the live and dead signals of all clusters within a single well and calculates a single viability value. However, in platforms with diverse cluster sizes, it is challenging to accurately assess the viability based on cluster size using such conventional methods (Figure 2.8B). To address this issue, we have developed an algorithm that can calculate the individual viability of diverse-sized clusters within a single well. This allows us to consider the diversity of organoid clusters and investigate the relationship between drug-induced growth rates and viability.

Confocal microscope images of tumor organoid microenvironment were taken as raw data with fluorescent green and red signals that represent tumor organoid clusters and dead cells, respectively. Images should be preprocessed because numerous noises interfere with the individual detection of tumor organoid clusters. Firstly, the overall brightness was adjusted through histogram equalization and normalization techniques. Then, blob removal and blur processes were carried out to denoise images to facilitate the contour detection of each cluster. Thereafter, the contour of clusters was separated independently, and individual cluster viability was measured by computing red signals overlapped with cluster area (green signals). Finally, average viability was quantified in groups classified by cluster size in

$500\mu m^2$ intervals. This method allows to figure out the relationship between cluster size and viability unlike conventional methods. Development of highly efficient quantitative analysis algorithm is expected to promote diverse approaches in experimental trends such as cell viability related with cluster size.

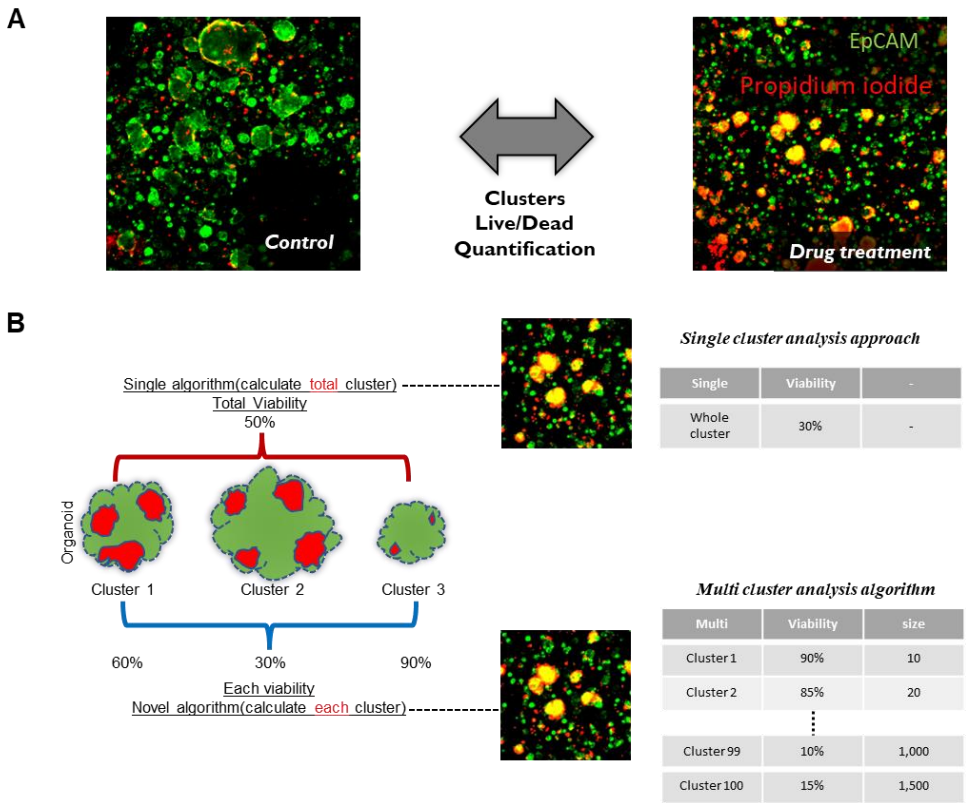

Figure 2.8. Organoid cluster analysis algorithm by computer vision. (A) The provided image depicts the Live/Dead assay results after drug treatment, showing clusters of varying sizes. Despite being composed of the same cells, we can observe differences in cell viability based on the cluster size. (B) The conventional approach involves analyzing a single cluster within a well and calculating overall viability by considering all the live and dead signals in the image together, which does not reflect the impact of cluster size. In contrast, the newly developed algorithm allows for the individual calculation of size-specific viability for each multi-cluster, enabling the extraction of their relationship. The results of the same image analyzed using the previous algorithm and the new algorithm shows that the new algorithm allows for a better understanding of the relationship between viability and size, enabling more

detailed analysis. On the other hand, the previous algorithm had difficulties in capturing such detailed information.

2.3.6. Drug treatment in vascularized patient-derived colorectal cancer in VT-MAP

We cultured clusters of various sizes on the VT-MAP platform to utilize the heterogeneity of organoids. Drugs for colorectal cancer (CRC), Oxaliplatin, Irinotecan and FOX (Combination of 5-Fu and Oxaliplatin) were used for drug treatment. The overall timeline of the drug treatment process is shown in Figure 2.9A. Initially, in the vascular area, a mixture of HUVECs and LFs was injected along with fibrin extracellular matrix. The remaining channels were filled with EGM-2 media, and we waited for two days for vascular development. We used two patient-derived xenograft models of colorectal cancer, namely CRC1 and CRC2. After two days, the media in the organoid area was aspirated, and CRC cells were injected along with HUVECs, CAFs, and fibrin extracellular matrix. After a day of stabilization, the drugs were mixed into the media. Following a two-day drug treatment period, the samples were fixed, and a Live/Dead assay was performed. Figure 2.9B shows the results of drug treatment.

CRC 1 and CRC 2 are colorectal patient-derived tumor organoid clusters that showed different reactions from drug treatments. CRC 1 is from a patient who completely recovered with anticancer drug treatment and CRC 2 is from a patient whose cancer was recurred after symptom relief and had resistance to anticancer drugs. Both patient-derived tumor organoid clusters were treated in 3D in vitro model using oxaliplatin, irinotecan and combination with 5-FU and oxaliplatin (FOX) for 2 days. CRC 1 and CRC2 showed a significant difference in the distribution data of cluster size and viability after drug treatment.

Figure 2.10A is a graph plotting the distribution of viability based on drug treatment results. In the case of CRC1, the viability under the control condition is high, while the samples treated with drugs show consistently low viability. On the other hand, for CRC2, not only the control condition but also all the drug-treated conditions show high viability. Figure 2.10B, on the other hand, represents the viability plotted based on the size of the clusters, rather than simply analyzing viability. For the control group, CRC 1 and CRC 2 agglomerated and grew in larger clusters with a wide range of size distribution up to about $6.0 \times 10^4 \mu m^2$ and $3.2 \times 10^4 \mu m^2$respectively, and high viability ranging from 80% to 95%. For the drug treated group, both in oxaliplatin 200μM and irinotecan 200μM, CRC1 clusters decreased in size as $2.0 \times 10^4 \mu m^2$at maximum and CRC2 clusters decreased as $1.0 \times 10^4 \mu m^2$ at maximum. However, CRC 1 showed 70% viability in small clusters and 20% viability in large clusters while CRC 2 showed high viability in 70%-85% in overall clusters. It implies that drugs suppressed the growth of cancer cells and lowered cell viability if cancer cells grew in large size for CRC 1. For combination treatment group, we observed drug performance in concentration with 50μM, 100μM, and 200μM. In case of CRC 1, cluster size was highly decreased under $1.0 \times 10^4 \mu m^2$ and cell viability was decreased from 80% to 20% as drug concentration increased from 50μM to 200μM. CRC 2 also showed decrease in size for all drug concentration as $1.0 \times 10^4 \mu m^2$ in maximum. In contrast to size distribution, the viability of CRC 2 clusters was between 70% to 90% for all conditions.

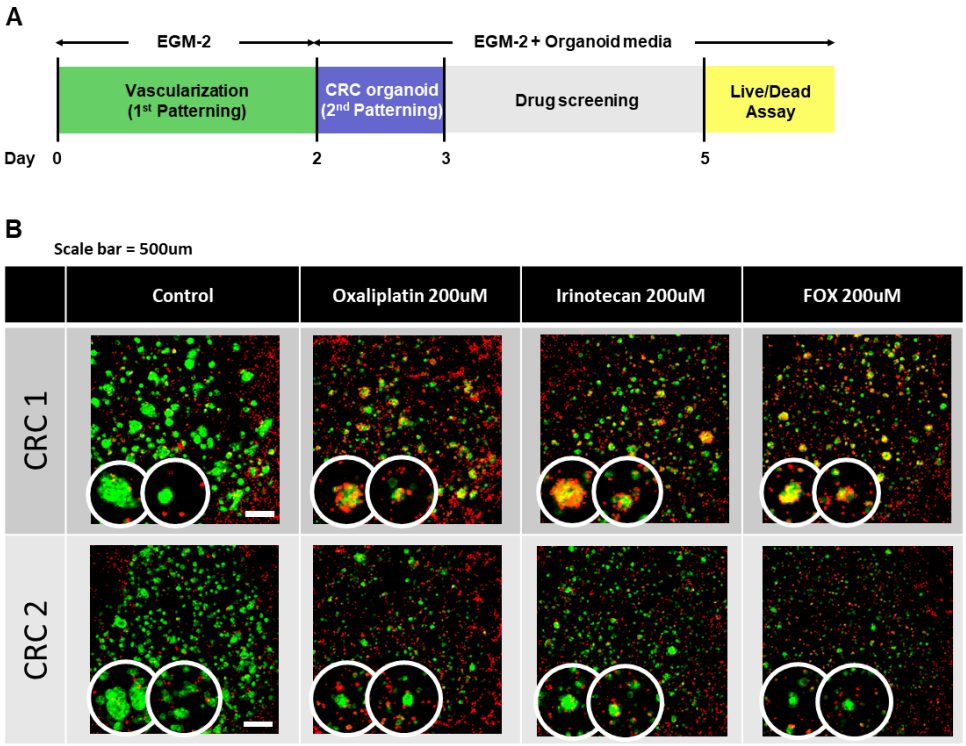

Figure 2.9. Drug screening process and Live/Dead assay results. (A) Drug treatment process on VT-MAP with multi clusters. (B) Drug screening results of CRC1 and CRC2. Control, Oxaliplatin, Irinotecan and FOX 200uM are shown in figures and specific images of each cluster.

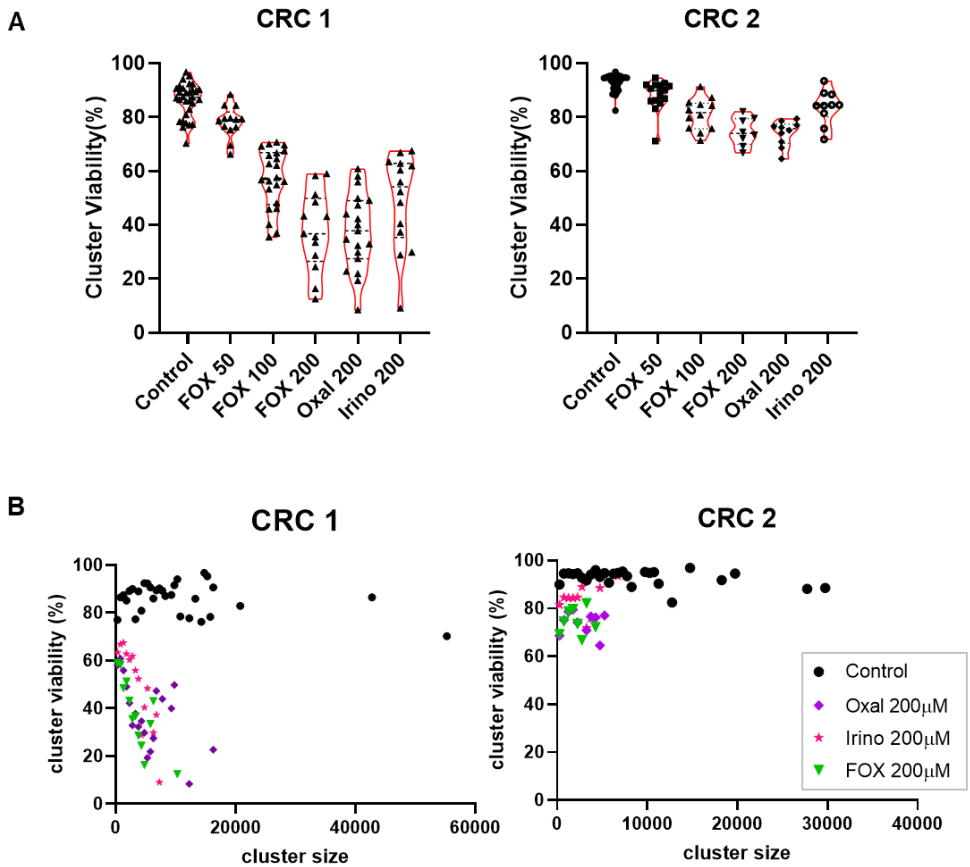

Figure 2.10. Drug screening results graph of CRC clusters. (A) Graph showed CRC1 and CRC2 clusters' viability distribution. The control condition of CRC1 exhibits high viability, while the viability decreases gradually in the drug-treated conditions. On the other hand, CRC2 shows high viability not only in the control condition but also in the drug-treated conditions, unlike CRC1. (B) The presented graph illustrates the variation in viability based on cluster size for CRC1 and CRC2. It visually demonstrates the changes in viability corresponding to different cluster sizes.

2.3.7. Comparing in-vivo and in-vitro results from VT-MAP

In the case of CRC1, the control condition exhibits high viability, while the treated conditions show a gradual decrease in viability. This suggests that CRC1 is sensitive to the drug treatment, resulting in a decrease in viability. On the other hand, both the control and treated conditions of CRC2 demonstrate high viability. This indicates that CRC2 either has a higher resistance to the drug treatment or there might exist different mechanisms of response to the drug. ,Therefore, CRC1 and CRC2 exhibit different patterns in terms of viability changes in response to drug treatment, suggesting differences in susceptibility or resistance to the drug on their respective aspects. As CRC 1 patient completely recovered and CRC 2 patient recurred after symptom relief, CRC 1 tumor organoid clusters highly reacted to drug treatment in cell size and viability and CRC 2 tumor organoid clusters only reacted in cell size maintaining high viability.

CRC1 and CRC2 are patient-derived cells obtained from Samsung Hospital, each with distinct characteristics. CRC1 represents cells from a patient who achieved remission through drug treatment, while CRC2 represents cells from a patient who experienced recurrence despite previous treatment. VT-MAP serves as an in vitro model capable of reflecting the unique characteristics of these patients. In the case of CRC1, we observe a decrease in both size and viability in response to drug treatment. This indicates a sensitive response to drugs as cells from a patient who achieved remission. On the other hand, CRC2 shows a decrease in size following drug treatment, but the viability remains relatively unaffected. This suggests an environment prone to recurrence. Conventional in vitro models could only observe low viability for both CRC1 and CRC2. However, VT-MAP provides more detailed

and complex information. It not only reveals changes in cell size and viability in response to drug treatment but also allows for the understanding of individual patient characteristics. VT-MAP bridges the gap between in vivo, ex vivo, and in vitro results, providing a platform to study personalized responses in a more comprehensive manner.

2.4. Discussion

This research highlights the current limitations of in-vitro models and underlines the urgent need for a more representative model to simulate the complex tumor microenvironment for large scale vascularized tissue or organoid models[38, 41, 77]. Organ-on-a-chip technology holds significant promise in this regard[15, 68], especially when paired with 3D vascularized tumor models[78]. This novel approach allows for a more nuanced investigation of cellular behaviors in a controlled, yet physiologically relevant, tumor microenvironment[79].

The development of a vascularized tumor model, however, remains a considerable challenge[20, 32, 80]. The intricate network of the vasculature and its physiological functions are complex to replicate in an in-vitro platform due to the small scale of current vascularized tumor on a chips. Combination of rail-assisted structure and mesh-assisted structure provides an enhanced platform for culturing large scale vascularized tissues or organoids within tumor microenvironment. Through this research, a large-scale vascularized tissue mesh-assisted platform (VT-MAP) have been developed. By leveraging fluid dynamics analysis derived from the previous rail-assisted approach, the limitations of scale hurdle have been overcome. Additionally, by introducing a new analysis method for multi-cluster's viability and size relationship.

Furthermore, VT-MAP demonstrates the potential to mimic the tumor microenvironment more realistically, which is characterized by dispersed clusters of various sizes rather than a single solid form. Unfortunately, most existing tumor drug screening models are limited to the culture of single spheroids in individual wells of a 96-well plate or tumor chip model. However, in this research, VT-MAP capable of

accommodating clusters of various sizes within the tumor microenvironment was proposed, allowing for a more realistic simulation of in vivo conditions. This platform provides an environment and space where hundreds of clusters can grow with diverse shapes and sizes within a single well. Moreover, the heterogeneity of the clusters provides an opportunity to observe drug responses based on growth rate and viability. VT-MAP have been successfully developed that allows for the extraction of diverse data from a single well.

VT-MAP and the new algorithm allow for a better understanding of the relationship between viability and cluster size, and enables more detailed analysis. In contrast, the previous algorithm had difficulties in capturing detailed information. These results demonstrate that the new algorithm has the ability to comprehensively analyze the relationship between cluster size and viability, providing valuable insights. Therefore, this research can contribute to a deeper understanding of organoid clusters and yield results that are more similar to in-vivo conditions.

2.5. Conclusion

In this research, we developed a large-scale vascularized tissue mesh-assisted platform called VT-MAP and evaluated organoids within it. This platform overcomes the limitations of the previous rail-assisted model‘s approach and enables efficient co-culture of large-scale tissues, including vascularized tissues or organoids. VT-MAP mimics the complex tumor microenvironment where clusters of various sizes and shapes grow and interact.

From the experimental results, VT-MAP has been demonstrated as a valuable tool for analyzing and interpreting various factors such as cluster size, viability, and drug responses. It allows for the investigation of the relationship between cluster size and viability, which was challenging in previous in-vitro models, and enables more detailed analysis. Importantly, the experimental results obtained with VT-MAP showed similarities to in-vivo conditions, distinguishing it from previous in-vitro models. This research contributes to the replication of a realistic tumor microenvironment and the investigation of cellular behaviors based on cluster size and viability using VT-MAP. Furthermore, VT-MAP accurately mimics the heterogeneity of organoid clusters and provides results that are more representative of in-vivo conditions, thus facilitating drug screening and drug screening research.

In conclusion, VT-MAP serves as a realistic and advanced platform for studying large scale vascularized tissues or organoids, offering new insights into the tumor microenvironment. It enhances our understanding of cancer treatment and tumor biology, and can be instrumental in the development of personalized therapeutic strategies.

Chapter 3. Deep Learning-driven Virtual Staining for High-throughput Microfluidic Angiogenesis Assays

3.1. Introduction

Organ-on-a-chip (OoC) technology has emerged as a promising platform for simulating human physiology and disease, with potential applications in drug screening and precision medicine. Microfluidic-based OoC systems have made progress in reproducing models of various organs similar to those *in vivo*, such as eyes [18, 81], intestines [82, 83], and tumor microenvironments [17, 38, 43]. However, their widespread adoption requires high-throughput screening capabilities, including mass device production, automated cell dispensing, and efficient data analysis [24]. Efforts are underway to increase compatibility with traditional laboratory equipment by integrating 3D co-culture systems within standard microplates [84, 85] and to improve robust cell dispensing methods through 3D printing and injection molding [44, 86, 87]. In particular, there are attempts to increase compatibility with existing labware or bioassays by building a cell co-culture system within a microplate standard [42, 88, 89].

Despite advances in high-throughput experimental equipment, effective data acquisition and analysis remain a challenge in the field [90-92]. Fluorescence imaging of OoC systems provides rich information, making functional parameter analysis important. However, the current analysis process, which involves cell fixation, fluorescence labeling, and confocal microscope, is cumbersome and time-consuming, with labeling results often yielding inconsistent results.

Recently, deep neural networks have been applied to image enhancement for immunocytochemistry research and medical imaging. Deep learning methods for image reconstruction, including convolutional neural networks (CNNs) and generative adversarial networks (GANs) [93, 94], have been used in a variety of biomedical images, such as super resolution microscope [95, 96], tumor segmentation in Magnetic Resonance (MR) images [97], and virtual histological staining [98-100]. However, deep learning technology is still not widely used in the field of OoC [101-104], owing in part to the difficulty of obtaining a large number of high-quality images for training [105].

In this study, we present the development of label-free fluorescent image construction techniques using a GAN-based SegNet architecture. The process was performed using large-scale, high-quality images obtained on the high-throughput microfluidic cell culture platform, the VS-IMPACT (Virtual Staining-assisted Injection Molded Plastic Array 3D Culture System). In particular, we demonstrate the virtual staining for the vasculature, one of the most morphologically complex organs in the human body. Our machine learning architecture, based on a large dataset, successfully reconstructs brightfield images into artificial fluorescence images, offering a promising tool for high-throughput screening in various disease models and drug response evaluation in the field of OoC.

3.2. Materials and Methods

3.2.1. Design and manufacturing process for VS-IMPACT platform

The injection molded angiogenesis platform was manufactured by injection molding. Polystyrene (PS) injection molding was performed at R&D Factory (Korea). The aluminum alloy mold core was machined by processing and polishing. The clamping force at injection was set at 130 ton at a maximum injection pressure of 55 bar, cycle time of 15 seconds, and a nozzle temperature of 220 ℃. The device was completely made by adhering a film substrate to an injection molded PS microfluidic body. The alloy mold core was designed by Solidworks at Dassault System.

3.2.2. Cell preparation

Human umbilical vein endothelial cells (HUVECs; Lonza, Switzerland) were cultured in endothelial growth medium 2 (EGM-2; Lonza), and the cell passage numbers between 4 and 5 were used for experiments. Lung fibroblasts (LFs; Lonza) were cultured in fibroblast growth medium 2 (FGM-2; Lonza), and cell passage numbers between 5 and 6 times were used for experiments. The cells were incubated at 37 °C in 5% CO2 for 2–3 days prior to chip loading. Cultured HUVECs and LFs were detached from the culture dish using 0.25% trypsin–EDTA (HyClone, USA). The various cells were then re-suspended in bovine fibrinogen solutions at the concentrations required for each experimental model.

3.2.3. Hydrogel and cell patterning

Prior to device seeding, every device was plasma surface treated at 70 W for 3 min to promote surface hydrophilicity (Femto Science, Korea). The central channel was patterned with 1 μl of acellular bovine fibrinogen solution (final concentration 2.5 mg/ml; Sigma, USA) which was added to 2% of bovine thrombin solution (0.5 U/ml, Sigma). Subsequently, 3 μl of the LFs (final concentration: 6 million cells/ml) and fibrinogen/thrombin mixture were patterned in the upper side channel. And the HUVECs suspension (final concentration: 3million cells/ml) was patterned in the lower side channel. Patterned chips were tilted until HUVECs were fully attached to the central acellular fibrin gel. Each media reservoir was filled with 100 μl of the growth medium after 15 minutes. The growth medium was changed every day. In order to generate shear stress and interstitial flow, all medium from the lower reservoir was removed and 100 μl of medium was injected only into the upper reservoir [106].

3.2.4. Immunocytochemistry

The samples in the device were fixed with 4% (w/v) paraformaldehyde (Biosesang, Korea) in PBS (Gibco, USA) for 15 min, followed by permeabilization with 20 minutes of immersion in 0.15% Triton X-100 (Sigma). The samples were then treated with 3% BSA (Sigma) for 1 h. Endothelial cell (EC)-specific staining was performed using 488 fluorescein-labeled Ulex Europaeus Agglutinin I (Vector, UK), which was prepared at a 1:500 ratio of dye in BSA for 12 h at 4 °C.

3.2.5. Image data collection and post processing

Imaging was performed using confocal microscope (Nikon Ti-2, Japan) to produce slice and z-stackable images of the angiogenesis for generating paired brightfield images and fluorescent images. High-throughput imaging software (Nikon High Content NIS-Elements Package, Japan) was used for high-speed, automated, well-plate formatted acquisition and efficient data management. Fiji (http://fiji.sc), an open-access software, was used to analyze the confocal images. Confocal 3D images were converted to 2D images by z-projection, then cropped to a defined region of interest.

3.2.6. Automatic image data analysis

For better data quantification, fluorescence images of angiogenesis had to be pre-processed. It was hard to get a clear result because the images had noise made by brightness variation, contrast difference, and tiny particles. The entire process of picture quantification is depicted in Figure 3.5. Image blurring was the first step in removing noise, which included averaging filtering, median filtering, Gaussian filtering, and so on, but in order to get the shape of the original vessel area, Gaussian filtering was used with the Python OpenCV library, which reliably preserved the value of the contour of vessels. The primary goal of gaussian filtering was to improve value uniformity, as fluorescent images of angiogenesis had nonuniform values overall. Following that, a proper threshold's binary value was entered to extract only the actual vessel area, compensating for the spreading of vessel value as blur and removing noise with a low fluorescence value. Even after Gaussian filtering and the binary threshold process, the angiogenesis image contained numerous black blobs

due to the nonuniformity of the value inside the angiogenesis area and white blobs from outside.

As a result, the algorithm in OpenCV with the Find-contour library was used to remove small islands or blobs of particles below a certain level of area. The skeletonization algorithm was used to extract a skeleton of 1 pixel size from a binary image of a vessel [107]. The total number of vessels and the number of angiogenesis endpoints may be easily determined using the vascular skeleton image. For rational counting of endpoints, our algorithm computed an average of the points' distances from the baseline in the top 20% of endpoints and set 50% of the average as the standard point to sort the endpoints that were growing more than others. The analytical algorithm enabled automatic quantification of the several parameters' tendency in images of angiogenesis. The entire quantification data were plotted by PRISM (GraphPad Prism 9).

3.2.7. Network architecture

A network structure based on the pix2pix network is used to convert unstained images into corresponding stained images. The network was configured based on SegNet instead of U-Net. Both networks have an encoder-decoder structure in common and consist of three paths. The first is the contracting path (left layers in **Figure 3.2**), which is composed of a continuous convolutional layer and a maxpooling layer and plays a role in capturing the overall context information of the image while continuously reducing the size of the image through downsampling. The second is an expansion path (right layers in Figure 3.2) that has the same symmetrical structure as a contracting path. It serves to up-sample the down-sampled image to its original size while passing through the contracting path. The third is the

skip connection path and corresponds to the red arrow connecting the contracting path and the expansive path in Figure 3.2. This path serves to provide information from a corresponding layer on a contracting path to a layer of an expansive path by one-to-one correspondence between the layers of the contracting path and the expansive path, so that the associated local information is included when performing upsampling.

The main difference between U-Net and SegNet is the difference in information provided through the connection path. In U-Net, the output of the corresponding layer on the reduced path is provided to the extension path through the connection path, and in the extension path, the transmitted information is concatenated with the output of the previous layer on the extension path [108]. On the other hand, in the case of SegNet, the index information of the maxpooling operation performed in the corresponding layer on the reduction path is transferred to the corresponding layer on the extension path, and in the extension path, upsampling is performed by inversely applying the index information [59]. In this paper, only the size of the input layer and the output layer were modified to fit the data. Since the encoder layers of SegNet are the same as the well-known VGG16 network, transfer learning was performed by applying the weight of the previously learned VGG16 network [109]. The hyperbolic tangent function tanh was applied as the activity function of the final layer. PatchedGAN technique was applied to the discriminator as shown in Figure 3.2. PatchedGAN is a technique in which the discriminator divides the image into small patches, determines the authenticity of each patch, and adopts the average of the discriminant values instead of discriminating the entire generated image.

3.3. Results

3.3.1. VS-IMAPCT: High-throughput screening using large-scale cell culture systems and deep learning-based virtual staining.

Conventional fluorescent staining for the angiogenesis model typically involves several procedures, including cell fixation, membrane permeabilization, blockage, and fluorescent antibody tagging. Additionally, widefield fluorescent microscope has limitations in detecting 3D organ structures over 100 mm in height. Our approach, on the other hand, employs a neural network architecture and a virtual fluorescent staining process that eliminates the need for conventional fluorescent staining or confocal microscope. Specifically, our architecture is trained to convert transmitted (brightfield) microscope images into fluorescent images, a process that takes only a few milliseconds per image (as shown in **Figure 3.1**A).

Machine learning-based image analysis typically requires hundreds of pairs of brightfield and fluorescence images, which can be challenging to obtain. To address this, we developed VS-IMPACT, which can achieve high-throughput screening using deep learning-based virtual staining of large-scale data obtained from injection-molded plastic array 3D culture platforms and automated data analysis (as shown in Figure 3.1C and D). The plate-scale microfluidic design we developed contained 28 samples, which has the potential to expand experimental yields for high throughput 3d cell culture (as shown in Figure 3.1B). Figure 3.1B shows the internal structure of each well, which consists of three microchannels: the center channel, lower channel, and upper channel.

We obtained image data from the VS-IMPACT platform using confocal microscope, which resulted in 1,036 paired, z-stacked images (brightfield and

fluorescent) that are each 512 x 512 pixels. Three images can be acquired in a single unit, and they are stitched together into a continuous image for integration of the complete image. The resulting image is resized to 1024 x 384 pixels for effective machine learning processing. We separated the dataset into training and test sets consisting of 828 and 208 pairs, respectively.

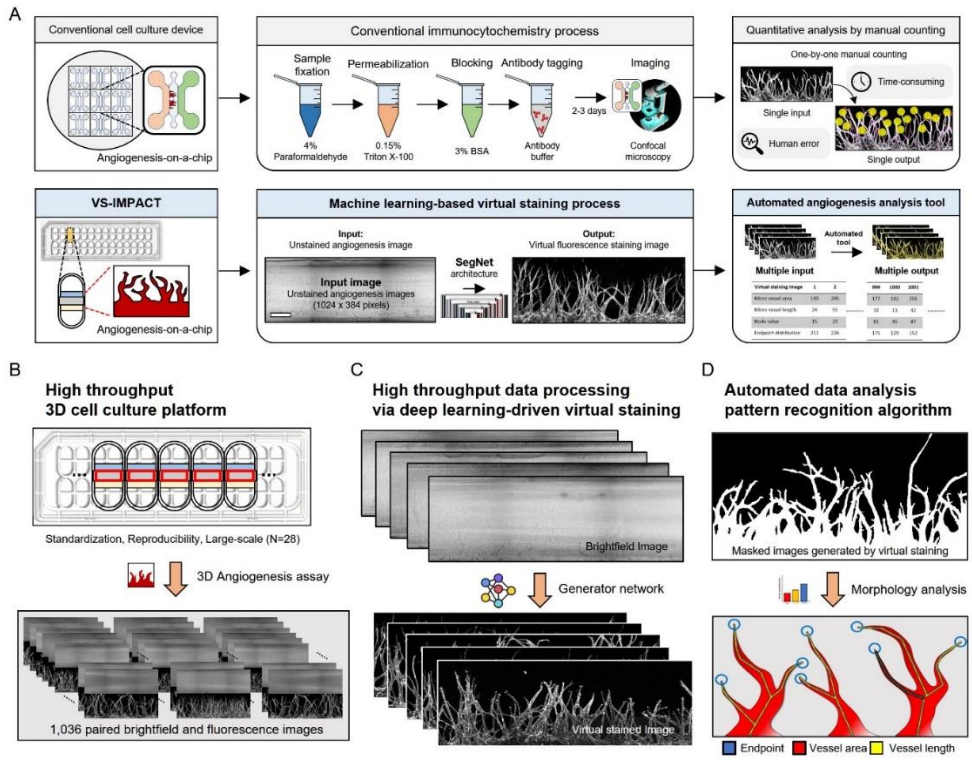

Figure 3.1. Workflow of deep learning-based virtual fluorescence staining and high throughput analysis. (A) Standard immunocytochemistry process with confocal microscope and virtual staining process for developing label-free fluorescent image. (B) Photographic and schematic image of VS-IMPACT chip. VS-IMPACT consists of 28 wells, accommodates high-throughput angiogenic sprout screening. Total of 1036 paired (brightfield, fluorescence) images were obtained. (C) High-throughput staining & imaging via deep neural network. (D) Angiogenesis analysis algorithm for evaluating virtual staining images. (Scale bar = 200μm)

3.3.2. Exploring neural network architectures for image conversion.

An encoder-decoder network is a neural network architecture where an encoder and a decoder are connected in a symmetrical manner, as shown in Figure 3.2. The encoder is responsible for encoding the input into a specific state, while the decoder generates the output from this state. Encoder-decoder networks are widely used for image conversion purposes, where the input image is transformed into another image having the same underlying structure. In an encoder-decoder network for image conversion, the encoder is usually composed of several convolutional layers, and the decoder is composed of symmetric layers as the encoder. The input image is downsampled while passing through successive layers of the encoder, and then upsampled again while passing through the decoding layers.

In most image conversion problems, the input and output images have a lot in common, and this common information needs to be passed to the output layer by skipping the network layers. To accomplish this, network structures that add a skip connection to the encoder-decoder network are used. U-Net or SegNet generates output by adding a skipping connection to the encoder-decoder structure and receiving global information from the encoded state and local information from the skipped connection. In the case of U-Net, the output of the corresponding layer is transmitted through the skipped connection, and in the case of SegNet, the index information of the max pooling operation is transmitted.

GAN is a neural network architecture based on Minmax game theory that optimizes the perceptual-level loss function by learning a generative model and an adversarial discriminative model simultaneously. GAN is widely used in the field of medical image processing, and its effectiveness has been proven for many problems such as image super-resolution reconstruction and brightfield holography.

Conditional GAN (cGAN) is the conditionalization of the generated model and the discrimination model with additional information in the GAN. The objective function of cGAN is expressed as follows.

$$\mathcal{L}_{cGAN}(G, D) = \mathbb{E}_{x,y}[\log D(x, y)] + \mathbb{E}_{x,z}[\log(1 - D(x, G(x, z)))]$$

Equation 5

Here, x and y are a pair of an image to be converted and a target image corresponding to the image, and z is a random vector. The generative model G minimizes this objective function for the hostile discriminator D, which aims to maximize this objective function. cGAN does not directly compare the image used for conditioning with the generated image. In other words, instead of directly providing a metric that determines how close the generated image is to the target image, it expects the discriminator to create such a criterion. On the other hand, in the pix2pix network, we directly add a loss function to the cGAN that represents the difference between traditional images, such as L1-distance. Unlike general cGAN applications, this is possible when a target image is present. That is, the objective function is as follows.

$$\mathcal{L}_{L1(G)} = \mathbb{E}_{x,y,z}[\|y - G(x, z)\|_1]$$

Equation 6

Our final objective is

$$G^* = arg \min_G \max_D \mathcal{L}_{cGAN}(G, D) + \lambda \mathcal{L}_{L1}(G).$$

Equation 7

In addition, the pix2pix network is different from cGAN in that it replaces the random vector z with the dropout layer and applies the PatchGAN technique to the discriminator. It is known that the PatchGAN has the effect of allowing the loss function to focus on precise details rather than the overall context of the image, that is, the high-frequency region of the image. This is related to the intention that the loss function comparing the target image and the generated image focuses on the overall contents of the image, and the discriminator focuses on the partial details of the image.

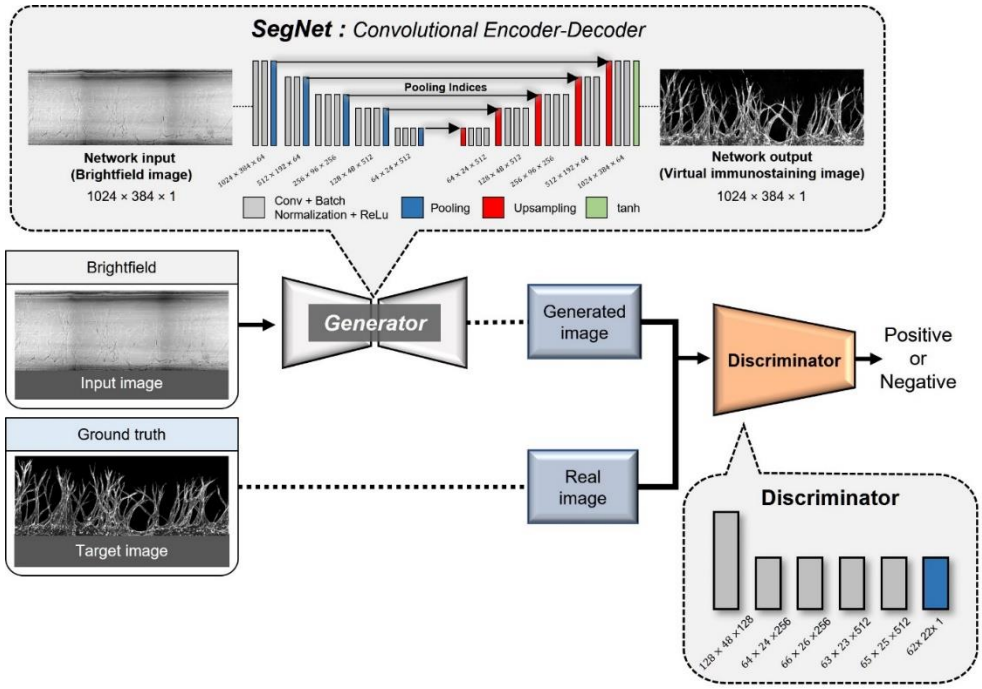

Figure 3.2. Structure of SegNet architecture design. Generator has an encoder-decoder structure based on SegNet network, which consist of three paths(contracting path, expansive path, skip connection path). Discriminator optimizes the perceptual-level loss function by learning a generative model and an adversarial discriminative model at the same time.

3.3.3. Loss functions for generating virtual immunostaining images of blood vessels.

The loss function is largely composed of GAN loss (L_{cGAN}), which expresses the discriminator's loss, and image loss (L_{image}), which compares the target image and the generated image. The choice of loss function is a key factor in the design of a neural network. For example, the most widely used traditional L2-norm is known to tend to produce rather blurry images. The pix2pix network applied the L1 loss function and showed that it produced a sharper image compared to L2. In addition to the traditional L1 and L2, there are metrics that focus on the perceptionally-motivated image. Representative examples include the structural similarity index (SSIM) and the multiscale structural similarity index (MS-SSIM). SSIM is a metric that reflects the intention to measure the perceived quality of an image. While traditional mean squared error (MSE) or peak signal-to-noise ratio (PSNR) measures absolute error, SSIM is a model that measures the perceived change in structural information of an image. Since the human visual system is specialized in deriving structural information from images, the degree of distortion of the structural information has the greatest effect on the perceived quality. SSIM is calculated for a constant-sized window on the image and averages them to calculate an estimate of the structural difference between the two images. For two windows x and y, SSIM is defined as follows. Here, μ_x and μ_y are the averages of the pixel values of x and y, respectively, ${\sigma_x}^2$ and ${\sigma_y}^2$ are the variance of the pixel values, σ_{xy} is the covariance, and c_1 and c_2 are constants for solving the division by zero error.

$$\boldsymbol{SSIM(x,y) = \frac{(2\mu_x\mu_y+c_1)(2\sigma_{xy}+c_2)}{(\mu_x^2+\mu_y^2+c_1)(\sigma_x^2+\sigma_y^2+c_2)}} \qquad \textbf{Equation 8}$$

Multiscale SSIM (MS-SSIM), an extended form of SSIM, is the addition of a scale space to SSIM, and after calculating SSIM at several scales, the final value is obtained by weighting it. As a result, the loss function considered in this paper can be expressed as follows.

$$L = w_{GAN} * L_{GAN} + w_{L1} * L^{L1} + w_{L2} * L^{L2} + w_{SSIM} * L^{SSIM} + w_{MS-SSIM} * L^{MS-SSIM}$$

Equation 9

In our study, we reconstructed virtually stained images for two SegNet-only conditions using L1 and L2 loss functions and four conditions with MS-SSIM, SSIM, L1, L2 loss and GAN loss added as described in **Figure 3.3A**. We called the images from the deep learning network "virtual immuno-staining images." Figure 3.3B demonstrates how the loss for each condition gradually decreases as epochs run. It begins to decline dramatically around epoch 50, then gradually declines. The loss value did not significantly decrease after epoch 150. Virtual immunostaining images were generated using the weight values at this point from the input image. The left side of **Figure 3.4** shows the result of generating the virtual staining image under six conditions. However, there are significant variations across the conditions when evaluating the micro vessel's characteristics, such as each endpoint, network, branch, and tortuosity. Therefore, it is necessary to confirm how much the difference between these images affects the analysis process.

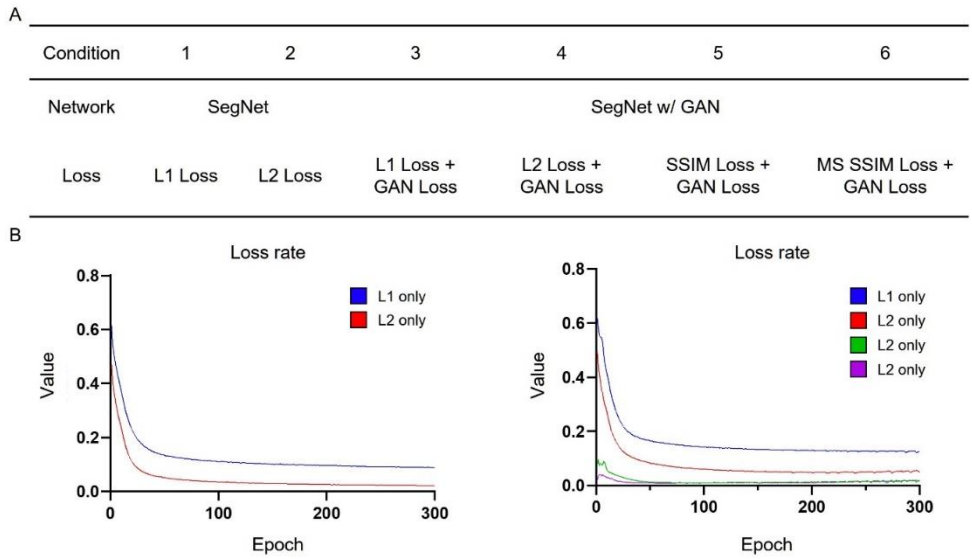

Figure 3.3. Virtual immunostaining images from various loss functions. (A) Loss function conditions from L1 and L2 loss only to L1, L2, SSIM and MS SSIM loss with GAN loss. (B) The values of loss functions were plotted with every epoch up to 300 epochs.

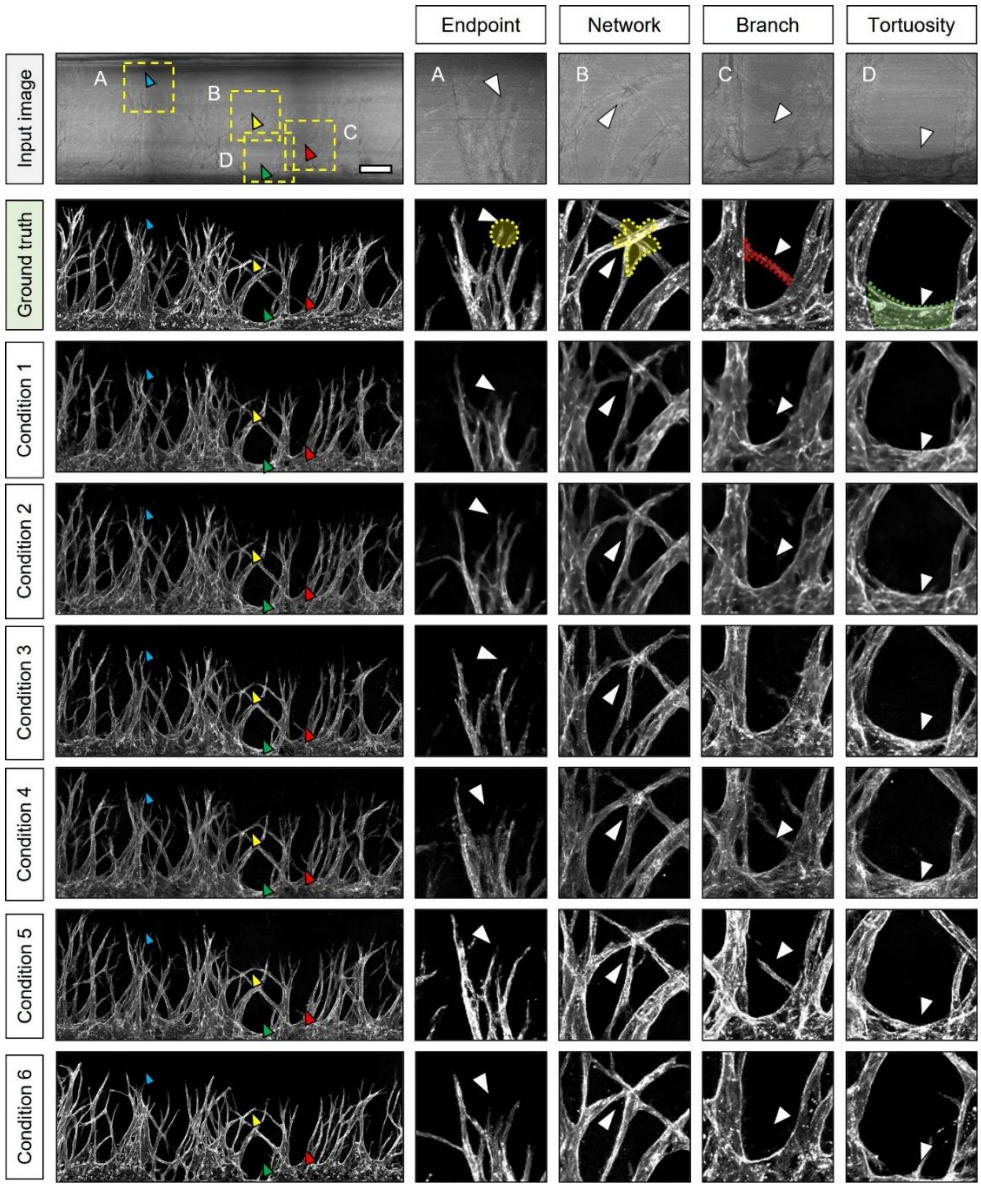

Figure 3.4. Detailed image between input, ground truth and virtual immunostaining images with different loss conditions. Enlarged comparison images between ground truth and virtual immunostaining images with (A) Endpoint, (B) Network (C) Branch and (D) Tortuosity. (GT: Ground truth, 1: L1 loss, 2: L2 loss, 3: L1 loss + GAN, 4: L2 loss + GAN, 5: SSIM + GAN, 6: MSSSIM + GAN, Scale bar = $\mathbf{200}\boldsymbol{\mu}$m)

3.3.4. Evaluating virtual immunostaining images using six loss conditions.

The difference between the input image, the GT, and the virtual image under six loss conditions is depicted in Figure 3.4. The image displays four distinct regions that highlight the major discrepancies in endpoint, network, branch, and tortuosity. The endpoint (Figure 3.4A) refers to the termination point of angiogenic sprouts, while the network (Figure 3.4B) represents the intersection point of the vascular networks. The branch (shown in Figure 3.4C) is the line that connects two vessels, and the tortuosity (shown in Figure 3.4D) is the main part of the vessel.

In some cases, the number of endpoints in the virtual fluorescent images may appear to be less clear than in the input image. This is because the endpoints in the input image are usually thinner than the main vessel. As the endpoints pass through the network, the information on their numbers is lost, causing them to move away from the GT image, as the white arrow in Figure 3.4A shows.

Despite these challenges, the virtual image successfully reproduces the morphology of the blood vessels, as can be seen in Figure 3.4B and 4C. The virtual blood vessel is implemented correctly when the input image vessel is thick, but details are lost when the input image vessel is thin. There is minimal error in the dominant blood vessel, with only the detail of the small blood vessel being lost, which does not significantly impact the quantitative analysis. However, in Figure 3.4D, the area disappears entirely due to the neural network's inability to adequately learn due to the input image's brightness, leading to a lower overall area value compared to the actual area.

Comparing the virtual immunostaining images to the GT images, the images have similar morphology macroscopically, but there are discrepancies in the level of

detail at the local scale. Conditions 1 to 6 in Figure 3.4 display the virtual immunostaining images with varying levels of detail. Conditions 1 and 2 depict a general vascular morphology, but the outline and interior of the vessels are blurred, with faint discoloration in luminance. The background and endpoint remain blurred, making it difficult to distinguish them clearly. Conditions 3 and 4 have a brighter interior and a slightly more distinct outline than conditions 1 and 2, but the endpoint still makes it challenging to distinguish between blurred endpoints and the black background.

Conditions 5 and 6, on the other hand, display a remarkable resemblance to the GT, with a prominent outline and a bright interior. The endpoints exhibit a distinct morphology and can be easily counted. Among the conditions, Condition 5 represents the optimal loss condition for application in virtual staining networks, as it implements a vessel morphology nearly identical to the GT.

3.3.5. Developing automated angiogenesis analysis algorithms.

In comparison to traditional 2D images, fluorescence images in OoC often exhibit higher levels of noise due to their three-dimensional nature. While the development of confocal microscopes has reduced noise caused by device thickness, excessive noise remains a challenge for efficient analysis (Figure 3.5). The accuracy of the image analysis tool and the labor-intensive analysis process are factors that have negatively impacted the usability of OoC. To address this issue, we present a method for reducing noise in stacked confocal images using the VS-IMPACT. This allows for the accurate recognition of blood vessel areas and a quick analysis of the number of sprouts, endpoints, and blood vessel length. The study processed 208 test images and applied a quantification algorithm to determine the results as shown in **Figure 3.6**A, which were then normalized against ground truth (GT) values. Figure 3.6B to 5D illustrate the normalized distribution of the virtual immunostaining images for each loss condition, where the X-axis represents loss conditions (L1, L2, L1 + GAN, L2 + GAN, SSIM + GAN, and MS-SSIM + GAN) and the Y-axis represents normalized values, with 1.0 being the ground truth standard. The average area value for each condition ranges from 0.74 to 0.95, with values for all conditions ranging from 0.60 to 1.20 (Figure 3.6B). Differences in area levels are attributed to differences in brightness between the internal area of the blood vessel and the ground truth, as shown in Figure 3.4. The range of length values is from 0.65 to 1.18, with a mean ranging from 0.77 to 1.00 (Figure 3.6C). The variation in endpoint values is greater than that of the other two parameters.

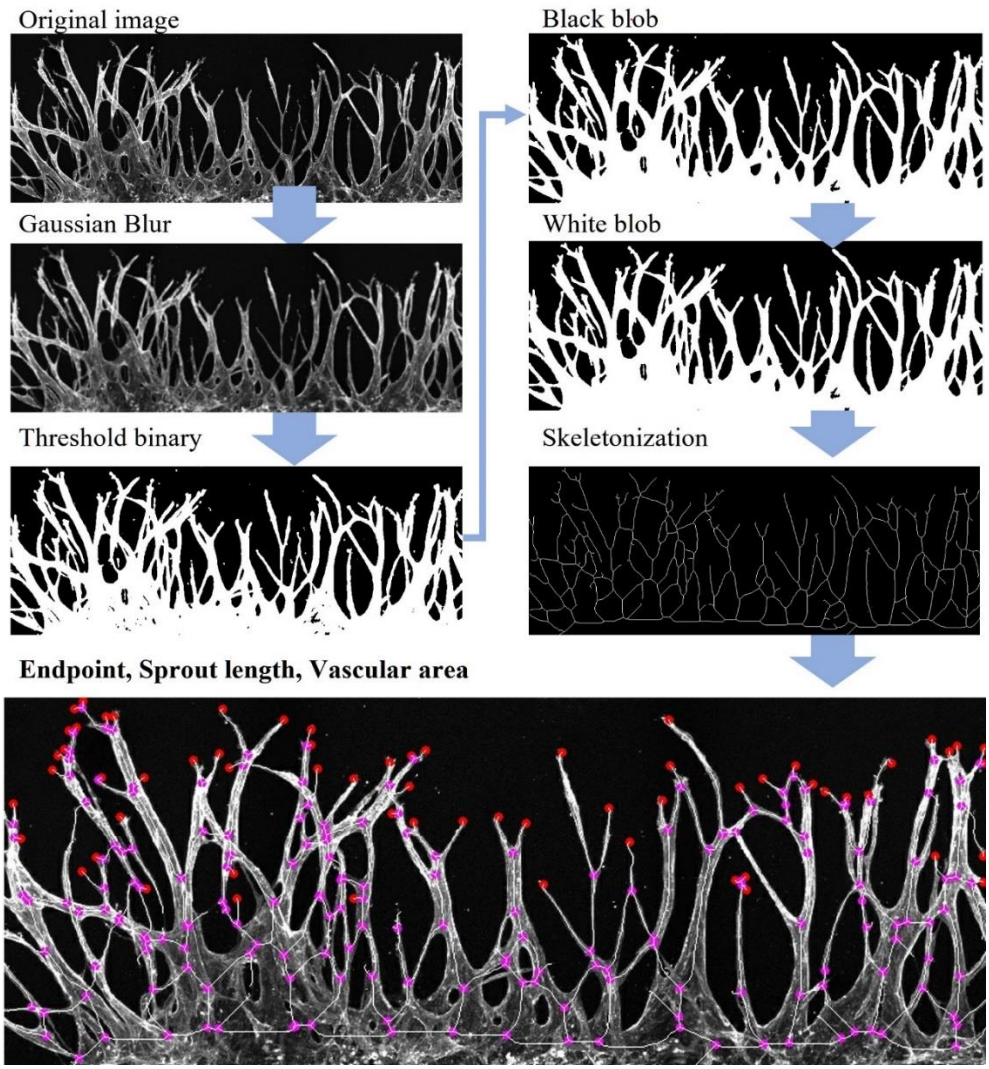

Figure 3.5. Angiogenesis quantification algorithm process. Start from preprocessing grayscale image by Gaussian Blur and Threshold binary to skeletonization network. Then skeletonization network is classified under three categories (sprout length, tip cell number, vascular area).

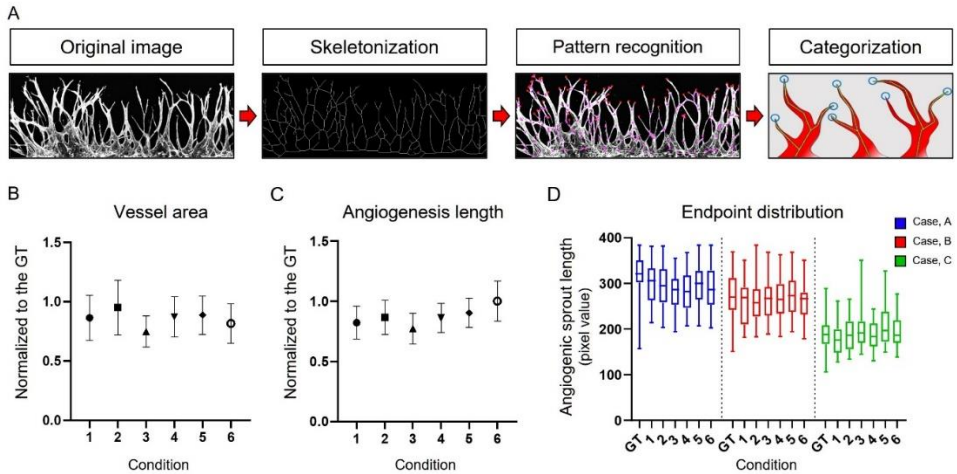

Figure 3.6. Evaluation of predicted model. (A) Angiogenesis quantification algorithm process for high-throughput analysis. (B) vessel area, (C) length and (D) endpoint sprout distribution number are plotted by box & whiskers with 208 test dataset in each condition. (GT: Ground truth, 1: L1 loss, 2: L2 loss, 3: L1 loss + GAN, 4: L2 loss + GAN, 5: SSIM + GAN, 6: MSSSIM + GAN)

3.3.6. Classifying endpoint distribution for accurate assessment of virtual immunostaining images.

To accurately assess the quantitative trend of virtual staining images, a new reference point, the endpoint sprout distribution, was introduced. The endpoint sprout distribution was used to quantify the actual degree of blood vessel growth, and its value was found to remain relatively unchanged even when the number of endpoints was altered. In this study, the endpoint sprout distribution was classified into three cases, A, B, and C, based on the length of the sprout and the size of the area (as shown in Figure 3.6D).

With a value of 318.55, case A had the highest average endpoint sprout for the GT. The distribution of average values for the six conditions when normalized to GT ranged from 88.44 to 94.01 %. Case B had an average GT of 269.92, with a distribution of six conditions ranging from 95.21 to 101.48 % when normalized to GT. Case C had the lowest average endpoint sprout among the cases, with a value of 188.44 for GT. The distribution of six conditions when normalized to GT ranged from 94.10 to 110.23 %. And all images of case A, B, and C with GT and six conditions are shown in **Figure 3.7**.

The results of the endpoint sprout inclination can be used as a metric to compare GT to other conditions. This approach allows for the average sprout distribution value of the test set to be quantified across all conditions.

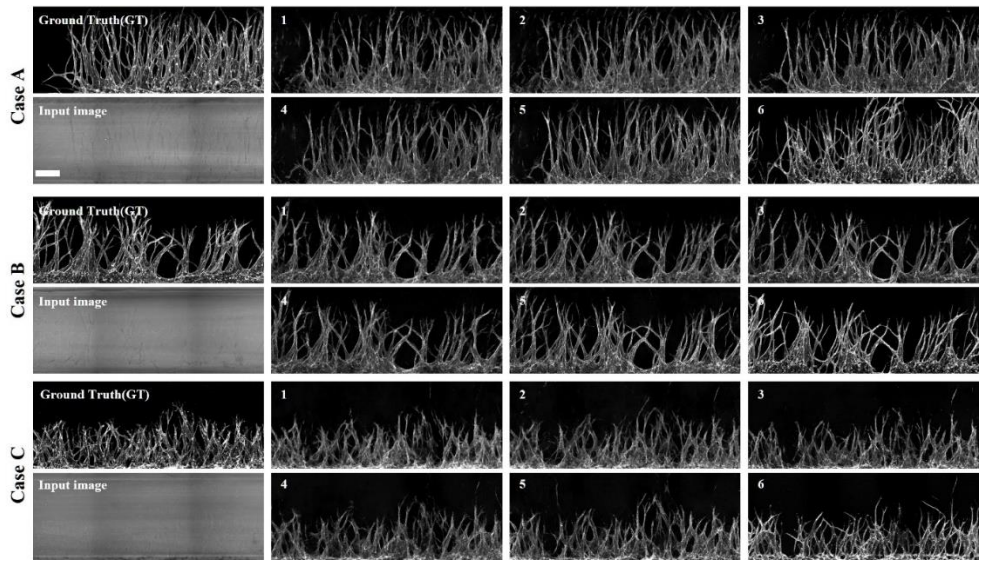

Figure 3.7. Input image, ground truth and six virtual immunostaining images from input images in case A, B and C with difference vessel growth height. (GT: Ground truth, 1: L1 loss, 2: L2 loss, 3: L1 loss + GAN, 4: L2 loss + GAN, 5: SSIM + GAN, 6: MSSSIM + GAN, $\mathbf{200}\boldsymbol{\mu}$m)

3.3.7. Evaluation of image quality and accuracy in loss functions for virtual images.

The accuracy of loss functions was assessed using image quality measurements based on L2 loss for each test set pair and total quantification data for area, length, and endpoint distribution. The mean square error (MSE) between the virtual images and the GT images was utilized as a metric for image quality evaluation (as shown in **Figure 3.8**A). The average MSE was 0.049, 0.048, 0.053, 0.050, 0.052, and 0.072 from condition 1 to 6, with conditions 1 to 5 having similar MSE values ranging from 0.048 to 0.052.

When analyzing the average quantification data of area, length, and number as shown in Figure 3.8B, it was found that condition 5 was the most accurate, with normalized values of 0.887, 0.903, and 1.015, respectively, which were all close to the ground truth value of 1.000. In comparison, condition 1 had values of 0.863, 0.822, and 0.945, while condition 2 had values of 0.951, 0.867, and 0.959. Condition 3 had values of 0.748, 0.774, and 0.975; condition 4 had values of 0.872, 0.862, and 0.951; and condition 6 had values of 0.816, 1.002, and 0.974. These values were generally lower compared to those in condition 5, indicating lower accuracy (Figure 3.8C).

In conclusion, condition 5 was found to have the highest accuracy among the six conditions in terms of area, length, and number measurements, as evidenced by its highest values for all three components. The other conditions had values that were generally lower, suggesting lower accuracy.

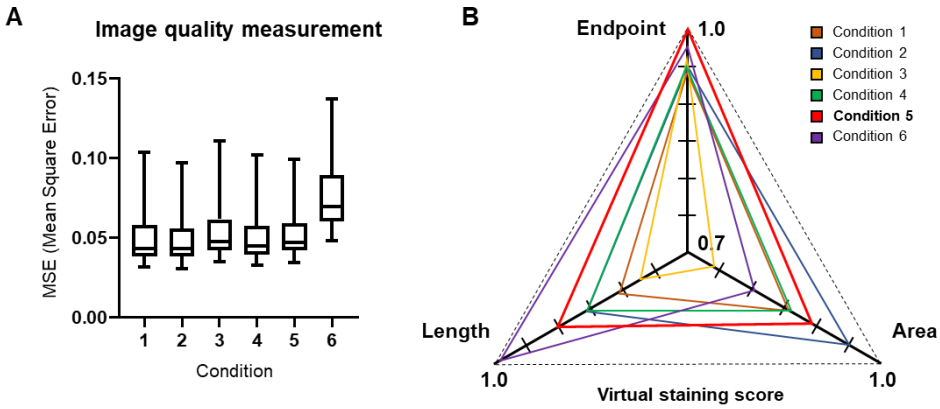

C

Condition	Endpoint	Length	Area	Total
1	0.945	0.822	0.863	0.876
2	0.959	0.867	0.951	0.925
3	0.975	0.774	0.748	0.832
4	0.951	0.862	0.872	0.895
5	**1.015**	**0.903**	**0.887**	**0.935**
6	0.974	1.002	0.816	0.930

Figure 3.8. Total quantification data normalized by ground truth. (A) Image quality measurement shows mean square error graph between ground truth images and virtual immunostaining images plotted by box & whiskers (B) The six conditions' quantification score are shown in three main components. (C) Total score of six conditions. (1 : L1 loss, 2 : L2 loss, 3 : L1 loss + GAN, 4 : L2 loss + GAN, 5 : SSIM + GAN, 6 : MSSSIM + GAN)

3.3.8. Virtual live cell imaging by optical microscope brightfield images

Applying virtual staining only to fixed samples is a good approach to address the bottleneck of the imaging system. However, it has the limitation of using data from a fixed state of the samples, making it difficult to obtain information about the previous stages of the process while angiogenesis step or vasculogenesis. To overcome this issue, we applied virtual staining to real-time live cell imaging. For live cell imaging, stitching the three images used in SegNet is inefficient, so we utilized single images obtained from the microscope (Figure 3.9A). The network suitable for the 1:1 ratio single image is a U-Net network based on the pix2pix architecture, which is commonly used in biological staining. We virtually stained and quantified the 1:1 ratio images of angiogenesis using both SegNet and U-Net for comparison (Figure 3.9B). The overall score of U-Net was 0.952, while SegNet scored 0.877. Therefore, we used U-Net for virtual staining of angiogenesis images at a 1:1 ratio.

In live cell imaging, confocal microscope is commonly used for high-quality results. However, confocal microscope, while providing high-quality fluorescent images, is not suitable for imaging many samples due to its high cost and slow performance. On the other hand, optical microscope is more affordable and offers faster performance, although the quality of fluorescent images is lower. Also, due to the size of the equipment, an optical microscope is ideal for observing sample growth in real time inside the incubator. Therefore, we suggested a strategy to combine the advantages of both types of microscopes. We utilized the brightfield and fluorescent image datasets obtained from the confocal microscope to train a U-Net network, creating a pre-trained virtual stain network. Through transfer learning,

we can input optical microscope brightfield images into this network to generate virtual staining images. These virtual staining images can mimic the fluorescent images from a confocal microscope when using an optical microscope (Figure 3.10) and enhance the quality of optical microscope images by virtually staining them with the characteristics of confocal microscope fluorescence images.

Figure 3.11A represents the results of virtual real-time live cell imaging. We installed an optical microscope inside the incubator to capture angiogenesis processes only using brightfield images, displaying the results at 10-hour intervals over a total of 50 hours. By comparing the virtual stained images with the brightfield images, we can accurately identify the vascular areas and observe the growth process clearly. For quantitative analysis, we quantified the virtual staining at one-hour intervals and presented the results in a graph in Figure 3.11B. This sample was not subjected to any separate drug treatment, and the area and length measurements show a linear increase, accurately reflecting the observed trends. The endpoint measurement reflects the gradual increase at the end of blood vessels, where differentiation does not occur continuously. The branch measurement, a parameter indicating the branching of blood vessels, demonstrates little change in more developed vessels, effectively capturing the observed pattern.

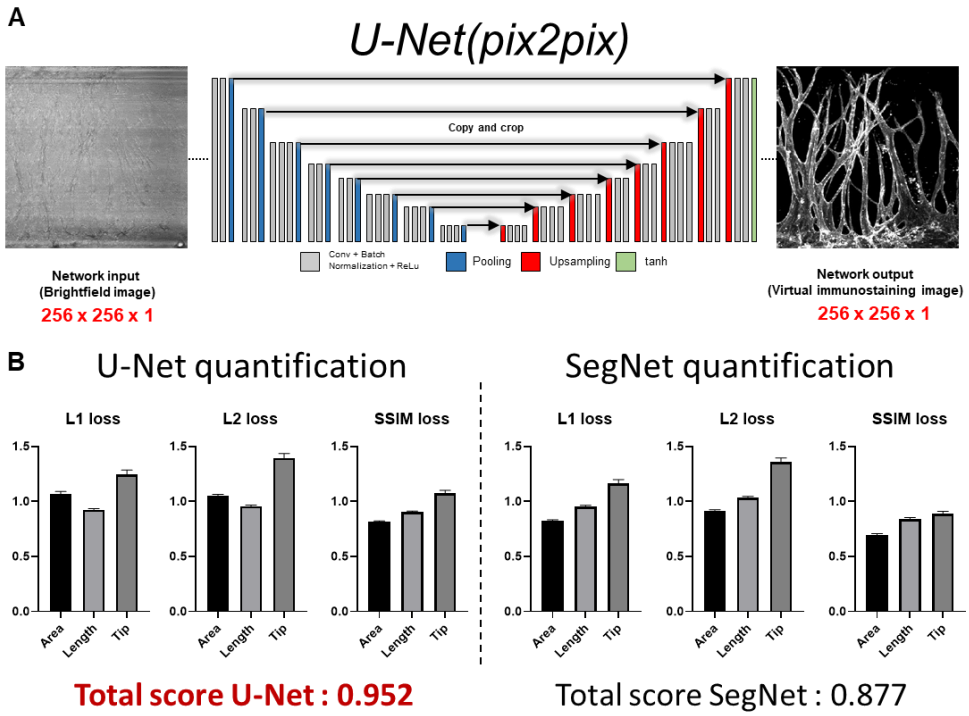

Figure 3.9. U-Net network based on pix2pix structure and quantification results between SegNet and U-Net. (A) U-Net network for 256 x 256 image set. Virtual live cell staining was challenging to apply in real-time with a 3 x 1 stitching approach. Therefore, the models were trained using single images of size 256 x 256. (B) U-Net and SegNet were trained on 256 x 256 images and compared based on quantitative analysis. The results revealed that U-Net outperformed SegNet, demonstrating superior performance in the task at hand.

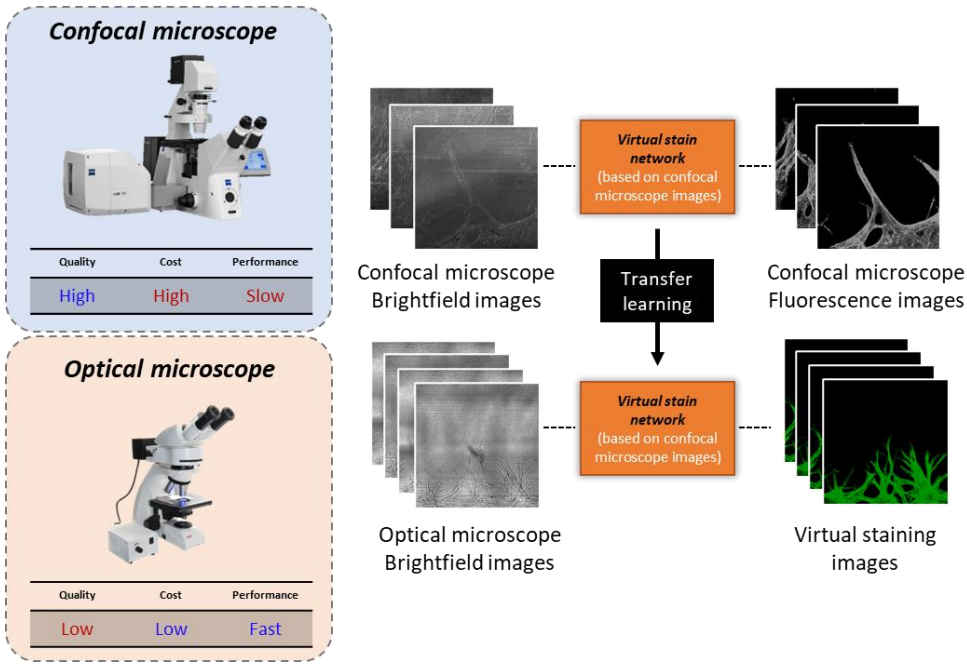

Figure 3.10. The differences between confocal and optical microscopes and transfer learning a network trained on a confocal microscope dataset to an optical microscope brightfield. It is a transfer learning that applies a virtual stain network trained with a confocal microscope dataset to optical microscope brightfield images. This enables virtual staining of confocal microscope fluorescence images with the quality of optical microscope brightfield images, which are easy to take, and can be used for real-time live cell imaging.

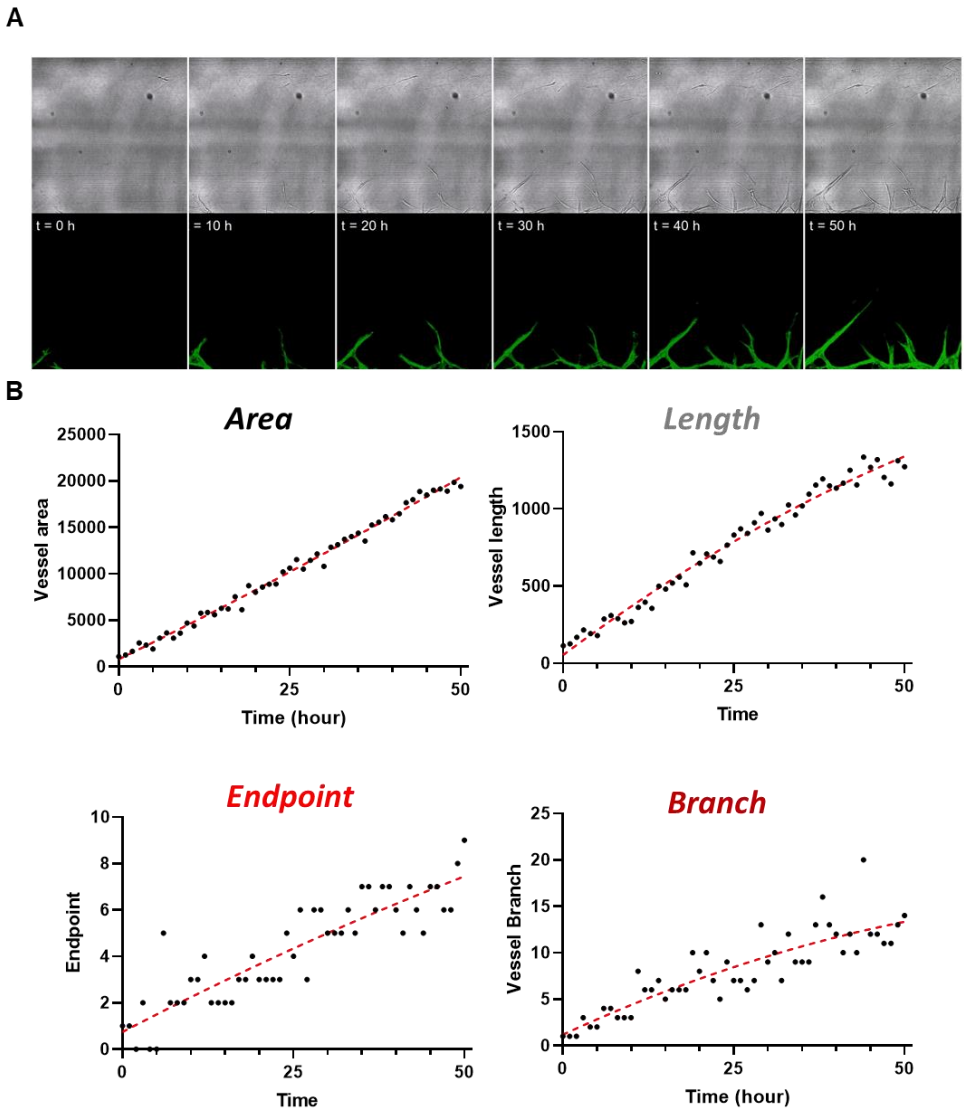

Figure 3.11. Virtual live cell imaging results and quantification. (A) The results show the application of virtual staining on real-time images captured at one-hour intervals during the angiogenesis process. We selected images at 10-hour intervals from the total of 50 hours to display. (B) This figure presents a graph plotting the four parameters of the actual blood vessels over time, quantified from the virtual live cell images. These four parameters are used to quantitatively measure the

characteristics of the blood vessels. It shows the changes over the course of 50 hours, allowing us to observe the trends for each parameter.

3.4. Discussion.

The utilization of OoC in drug development and as a preclinical model is the subject of ongoing discussions. One of the challenges that remains to be addressed is the standardization of data analysis [24, 110, 111]. The data analysis process in OoC is prone to errors due to various factors that influence the image generation and analysis process. To address this issue, machine learning techniques are being applied to perform morphological analysis of cells or organoids with simple structures [112, 113]. In this study, we have successfully applied machine learning morphological analysis to one of the most complex organs, the vasculature.

The complexity of the micro-vascular structure, including networks, endpoints, and tortuosity, presents numerous factors to consider in the morphological analysis of 3D blood vessels. Furthermore, the uneven brightness of the 3D vessel images makes it difficult to acquire precise blood vessel data through straightforward skeletonization. To overcome these challenges, we developed an algorithm that enhances the quantification method and preprocessing steps to provide more accurate data. The integration of mass producible OoC, deep neural networks, and analytics algorithms streamlines protocols and shortens the process.

Our study developed a high-throughput analysis process that uses widely adopted elimination, skeletonization, and binarization techniques. Our algorithm analyzes the number of endpoints, length, and area of angiogenesis, which are used as standard indicators for vascular morphology analysis. The images generated by deep learning were used to verify the results of the algorithm. Through the deep learning architecture with six objective functions, we generated 208 pairs of test images. A qualitative evaluation showed the most images in the six conditions maintained the overall shape and branching structure, although there was some loss

of detailed information compared to the ground truth image. The model without GAN loss weighting showed significant differences from the actual fluorescence image, while the GAN loss-weighted model was difficult to distinguish from the actual stained image, especially with the SSIM and MS-SSIM loss models (Figure 3.4).

Traditional manual counting methods and commonly used angiogenesis evaluation tools, such as AngioTool [114, 115], are labor-intensive and subjective, requiring different parameters for each image. These tools are also limited to flat 2D blood vessels, making it challenging to evaluate 3D blood vessel data. Our system, VS-IMPACT, provides a specialized analysis tool for 3D blood vessels, from imaging to quantification. The system's method can replace the current immunocytochemistry process, allowing for non-destructive real-time imaging and the evaluation of 3D vasculature characteristics, which is useful for high-throughput drug screening and creating a visible microenvironment. Additionally, the non-destructive real-time imaging enables the end-user to continuously track the growth of a 3D micro-vascular network while acquiring quantitative data.

Our research significantly shortened the data acquisition and analysis processes in OoC. We acquired many images of complex vascular networks using the high-throughput VS-IMPACT. Brightfield images were quickly acquired without fluorescence filters or lasers, and the vascular network was specified through the virtual staining process using the deep learning architecture. This algorithmic analysis tool measures the morphological characteristics of angiogenesis without human intervention, establishing a standardized protocol for data processing in OoC, leading to significant time savings and error reduction.

Moreover, we explored the potential and usefulness of virtual live cell imaging. We performed brightfield imaging using a real-time microscope and generated virtual stained images using U-Net. Through this approach, results like confocal microscope fluorescence images were obtained from an optical microscope. Additionally, by quantifying and graphing the four parameters of the actual blood vessels, we were able to accurately track the growth and differentiation processes of the angiogenesis. These results demonstrate the feasibility of virtual staining in the field of real-time live cell imaging and highlight the utility of combining the advantages of optical microscope with the fluorescence imaging quality of confocal microscope. Therefore, virtual staining for real-time microscope imaging holds great promise as an important tool in biological research and medical applications.

3.5. Conclusion.

In this study, we aimed to advance high-throughput OoC experimentation by introducing the innovative VS-IMPACT platform. This platform allows us to obtain large-scale brightfield images of target objects without the use of fluorescent staining. The images undergo a deep learning-based virtual staining process and virtual live cell imaging that characterizes the objects as if they were stained using traditional methods. Additionally, we optimized our algorithmic measurement tool to provide automated morphological analysis, eliminating the need for manual intervention. We successfully demonstrated the feasibility and efficacy of our approach through its application to the complex structure of 3D blood vessels. Our proposed model has the potential to streamline post-processing steps in various fields of cell culture research, including OoC experiments. Furthermore, the non-destructive real-time analysis of living cells offers various avenues for analysis, such as evaluating immune-mediated tumor killing.

Chapter 4. Concluding remarks

In recent years, organ-on-a-chip technology has emerged as a transformative approach for advancing drug development and precision medicine. Organ chips, also known as microphysiological systems, are innovative platforms that aim to replicate the structural and functional characteristics of human organs in vitro. These microfluidic devices offer a unique opportunity to study complex biological processes by incorporating various cell types and mimicking the physiological conditions found in vivo. Organ chips have revolutionized traditional in vitro models by providing a more accurate representation of human physiology compared to conventional cell culture systems. They enable the integration of multiple cell types, including parenchymal cells, endothelial cells, and immune cells, allowing for the recreation of organ-specific microenvironments. By recapitulating the organ's architecture, cell-cell interactions, and tissue-specific functions, organ chips provide a sophisticated tool for studying organ-level responses and drug effects.

Despite their tremendous potential, organ chips face certain limitations that need to be addressed. One notable challenge is the development of vascularized tissue models within organ chips. The inclusion of functional blood vessels is crucial for replicating the complex physiological processes that occur within organs. While existing vascularized spheroid models have been successful in co-culturing small-scale tumors, they are not well-suited for achieving large-scale vascularized organoid models. This limitation hinders the scalability and clinical relevance of these models.

In chapter 2, to address the limitations of existing organ chip technology, I propose the Vascularized Tissue Mesh-Assisted Platform (VT-MAP) as an innovative solution. The VT-MAP combines the advantages of the existing rail-

assisted structure with the mesh-assisted structure, enabling the development of large-scale vascularized tissue or organoid models. By incorporating both structures, VT-MAP offers enhanced scalability and adaptability, making it well-suited for accommodating the complex and dynamic nature of vascularized tissues. VT-MAP holds great promise in advancing drug screening and precision medicine research. It provides an environment that closely resembles in vivo and ex vivo conditions, offering a valuable tool for studying the drug response evaluation of cells in a more physiologically relevant context. By maintaining high reproducibility and scalability, VT-MAP enables the investigation of large-scale vascularized organoid models, bridging the gap between traditional in vitro models and the complexity of in vivo systems. This platform not only allows for the cultivation of vascularized tissues or organoids but also facilitates the study of various biological processes, including angiogenesis, tissue development, and disease progression.

The implementation of VT-MAP in drug development and precision medicine research offers exciting opportunities to improve our understanding of human physiology and advance therapeutic interventions. By overcoming the limitations of existing models, VT-MAP provides a powerful tool for studying complex biological systems and evaluating drug efficacy and safety with higher accuracy and reliability. With its ability to replicate large-scale vascularized tissue models, VT-MAP has the potential to transform the field of organ-on-a-chip technology and drive advancements in personalized medicine and drug discovery.

Another limitation lies in the imaging systems used in these platforms. As throughput has increased, imaging systems, particularly confocal microscopes commonly used in organ chips, have struggled to keep up with the growing demand. Cost and performance limitations have resulted in a bottleneck in capturing all the

necessary data. To address these limitations, I propose a solution in chapter 3. The thesis introduces the Virtual Staining-assisted Injection Molded Plastic Array 3D Culture System (VS-IMPACT), a high-throughput microfluidic system that leverages deep learning-based virtual staining techniques. The VS-IMPACT platform integrates various processes, ranging from large-scale image data acquisition to quantitative analysis of angiogenesis, providing a valuable tool for pharmaceutical and biological research. With the capability to transform brightfield images into label-free virtual fluorescence images, VS-IMPACT eliminates the need for traditional staining methods, enabling effective live cell imaging without the cell fixation process. This revolutionary approach not only improves experimental efficiency but also allows for the evaluation of responses to angiogenesis inhibitors or anticancer drugs in the tumor microenvironment. By providing reliable and reproducible vascular images, VS-IMPACT offers a high-throughput solution for studying angiogenesis and its modulation in the context of tumor development and treatment.

Moreover, I have extended the concept of virtual staining and integrated it with a live cell imaging system, enabling the establishment of real-time virtual live cell imaging using only brightfield images. Unlike conventional methods that require fixing the samples at specific time points, our approach allows for the acquisition of data throughout the entire growth process of the samples. By eliminating the need for immunocytochemistry process for cell staining, we can obtain valuable data without any damage of the samples, providing a significant competitive advantage. The introduction of virtual live cell imaging opens new possibilities for studying dynamic cellular processes and interactions. Researchers can now observe and analyze the growth, migration, and behavior of cells in real-time within a

vascularized microenvironment, enabling a comprehensive understanding of complex biological phenomena. This innovative approach not only improves the efficiency and accuracy of data acquisition but also offers insights into the cellular dynamics that were previously inaccessible. By combining the benefits of virtual staining and live cell imaging, we have established a powerful tool for studying cellular behavior and advancing our understanding of disease mechanisms, ultimately contributing to the fields of biological research, drug discovery, and precision medicine.

In summary, the development of VT-MAP and VS-IMPACT represents significant advancements in the field of organ-on-a-chip technology. These innovative platforms address the limitations of existing models, providing scalable and high-throughput solutions for studying vascularized tissue models and angiogenesis. By bridging the gap between in vitro and in vivo systems, VT-MAP and VS-IMPACT offer valuable tools for drug screening, precision medicine, and biological research, contributing to advancements in therapeutic interventions and our understanding of complex biological processes. By addressing the limitations of current in vitro models and leveraging these innovative approaches, the thesis holds great potential for advancing drug development and precision medicine research.

Bibliography

1. Robinson, N.B., et al., *The current state of animal models in research: A review.* International Journal of Surgery, 2019. **72**: p. 9-13.
2. Wu, Q.R., et al., *Organ-on-a-chip: recent breakthroughs and future prospects.* Biomedical Engineering Online, 2020. **19**(1).
3. Ma, C., et al., *Organ-on-a-chip: a new paradigm for drug development.* Trends in pharmacological sciences, 2021. **42**(2): p. 119-133.
4. Zhang, B.Y., et al., *Advances in organ-on-a-chip engineering.* Nature Reviews Materials, 2018. **3**(8): p. 257-278.
5. Pampaloni, F., E.G. Reynaud, and E.H. Stelzer, *The third dimension bridges the gap between cell culture and live tissue.* Nat Rev Mol Cell Biol, 2007. **8**(10): p. 839-45.
6. Kapalczynska, M., et al., *2D and 3D cell cultures - a comparison of different types of cancer cell cultures.* Arch Med Sci, 2018. **14**(4): p. 910-919.
7. Costa, E.C., et al., *3D tumor spheroids: an overview on the tools and techniques used for their analysis.* Biotechnol Adv, 2016. **34**(8): p. 1427-1441.
8. Ravi, M., et al., *3D cell culture systems: advantages and applications.* J Cell Physiol, 2015. **230**(1): p. 16-26.
9. Leung, C.M., et al., *A guide to the organ-on-a-chip.* Nature Reviews Methods Primers, 2022. **2**(1): p. 33.
10. Huh, D., et al., *Microfabrication of human organs-on-chips.* Nature protocols, 2013. **8**(11): p. 2135-2157.
11. Kim, S., et al., *Interstitial flow regulates the angiogenic response and phenotype of endothelial cells in a 3D culture model.* Lab on a Chip, 2016. **16**(21): p. 4189-4199.
12. Clay, N.E., et al., *Modulation of matrix softness and interstitial flow for 3D cell culture using a cell-microenvironment-on-a-chip system.* ACS Biomaterials Science & Engineering, 2016. **2**(11): p. 1968-1975.
13. Wevers, N.R., et al., *A perfused human blood–brain barrier on-a-chip for high-throughput assessment of barrier function and antibody transport.* Fluids and Barriers of the CNS, 2018. **15**(1): p. 1-12.
14. Ingber, D.E., *Human organs-on-chips for disease modelling, drug development and personalized medicine.* Nature Reviews Genetics, 2022. **23**(8): p. 467-491.
15. Ahn, J., et al., *3D microengineered vascularized tumor spheroids for drug delivery and efficacy testing.* Acta Biomater, 2022.
16. Lai, B.F.L., et al., *Recapitulating Pancreatic Tumor Microenvironment through Synergistic Use of Patient Organoids and Organ-on-a-Chip Vasculature.* Advanced Functional Materials, 2020. **30**(48): p. 2000545.

17. Nashimoto, Y., et al., *Vascularized cancer on a chip: The effect of perfusion on growth and drug delivery of tumor spheroid.* Biomaterials, 2020. **229**.
18. Ragelle, H., et al., *Human Retinal Microvasculature-on-a-Chip for Drug Discovery.* Advanced Healthcare Materials, 2020. **9**(21).
19. Shin, N., et al., *Vascularization of iNSC spheroid in a 3D spheroid-on-a-chip platform enhances neural maturation.* Biotechnology and Bioengineering, 2022. **119**(2): p. 566-574.
20. Phan, D.T., et al., *A vascularized and perfused organ-on-a-chip platform for large-scale drug screening applications.* Lab on a Chip, 2017. **17**(3): p. 511-520.
21. Park, J., et al., *Enabling perfusion through multicellular tumor spheroids promoting lumenization in a vascularized cancer model.* Lab on a Chip, 2022. **22**(22): p. 4335-4348.
22. Kim, D., et al., *Vascularized lung cancer model for evaluating the promoted transport of anticancer drugs and immune cells in an engineered tumor microenvironment.* Advanced Healthcare Materials, 2022. **11**(12): p. 2102581.
23. Vladisavljevic, G.T., et al., *Industrial lab-on-a-chip: Design, applications and scale-up for drug discovery and delivery.* Advanced Drug Delivery Reviews, 2013. **65**(11-12): p. 1626-1663.
24. Leung, C.M., et al., *A guide to the organ-on-a-chip.* Nature Reviews Methods Primers, 2022. **2**(1).
25. Shin, J., et al., *Monolithic digital patterning of polydimethylsiloxane with successive laser pyrolysis.* Nature Materials, 2021. **20**(1): p. 100-107.
26. Razavi Bazaz, S., et al., *Rapid softlithography using 3D-printed molds.* Advanced materials technologies, 2019. **4**(10): p. 1900425.
27. Homan, K.A., et al., *Flow-enhanced vascularization and maturation of kidney organoids in vitro.* Nature methods, 2019. **16**(3): p. 255-262.
28. Lee, U.N., et al., *Fundamentals of rapid injection molding for microfluidic cell-based assays.* Lab on a Chip, 2018. **18**(3): p. 496-504.
29. Lerman, M.J., et al., *The evolution of polystyrene as a cell culture material.* Tissue Engineering Part B: Reviews, 2018. **24**(5): p. 359-372.
30. Khetani, S.R. and S.N. Bhatia, *Microscale culture of human liver cells for drug development.* Nature biotechnology, 2008. **26**(1): p. 120-126.
31. Zheng, F.Y., et al., *Organ-on-a-Chip Systems: Microengineering to Biomimic Living Systems.* Small, 2016. **12**(17): p. 2253-2282.
32. Yu, J., et al., *Perfusable micro-vascularized 3D tissue array for high-throughput vascular phenotypic screening.* Nano Convergence, 2022. **9**(1): p. 16.
33. Toh, Y.C., et al., *A microfluidic 3D hepatocyte chip for drug toxicity testing.* Lab Chip, 2009. **9**(14): p. 2026-35.

34. Banaeiyan, A.A., et al., *Design and fabrication of a scalable liver-lobule-on-a-chip microphysiological platform.* Biofabrication, 2017. **9**(1): p. 015014.
35. Murphy, S.V. and A. Atala, *3D bioprinting of tissues and organs.* Nat Biotechnol, 2014. **32**(8): p. 773-85.
36. Mandrycky, C., et al., *3D bioprinting for engineering complex tissues.* Biotechnology Advances, 2016. **34**(4): p. 422-434.
37. Zhang, Y.S., et al., *Bioprinting 3D microfibrous scaffolds for engineering endothelialized myocardium and heart-on-a-chip.* Biomaterials, 2016. **110**: p. 45-59.
38. Shirure, V.S., et al., *Tumor-on-a-chip platform to investigate progression and drug sensitivity in cell lines and patient-derived organoids.* Lab on a Chip, 2018. **18**(23): p. 3687-3702.
39. Wang, Y., et al., *Engineering stem cell-derived 3D brain organoids in a perfusable organ-on-a-chip system.* RSC advances, 2018. **8**(3): p. 1677-1685.
40. van Duinen, V., et al., *Microfluidic 3D cell culture: from tools to tissue models.* Current Opinion in Biotechnology, 2015. **35**: p. 118-126.
41. Brandenberg, N., et al., *High-throughput automated organoid culture via stem-cell aggregation in microcavity arrays.* Nature biomedical engineering, 2020. **4**(9): p. 863-874.
42. Kim, Y., et al., *All-in-one microfluidic design to integrate vascularized tumor spheroid into high-throughput platform.* Biotechnology and Bioengineering, 2022. **119**(12): p. 3678-3693.
43. Ko, J., et al., *Tumor spheroid-on-a-chip: a standardized microfluidic culture platform for investigating tumor angiogenesis.* Lab on a Chip, 2019. **19**(17): p. 2822-2833.
44. Lee, B., et al., *3D micromesh-based hybrid bioprinting: multidimensional liquid patterning for 3D microtissue engineering.* Npg Asia Materials, 2022. **14**(1).
45. Hofer, M. and M.P. Lutolf, *Engineering organoids.* Nat Rev Mater, 2021. **6**(5): p. 402-420.
46. Jain, R.K., et al., *Engineering vascularized tissue.* Nat Biotechnol, 2005. **23**(7): p. 821-3.
47. Kirkpatrick, C.J., S. Fuchs, and R.E. Unger, *Co-culture systems for vascularization--learning from nature.* Adv Drug Deliv Rev, 2011. **63**(4-5): p. 291-9.
48. Vijayavenkataraman, S., et al., *3D bioprinting of tissues and organs for regenerative medicine.* Adv Drug Deliv Rev, 2018. **132**: p. 296-332.
49. Zhang, S., Z. Wan, and R.D. Kamm, *Vascularized organoids on a chip: strategies for engineering organoids with functional vasculature.* Lab Chip, 2021. **21**(3): p. 473-488.

50. Peel, S., et al., *Introducing an automated high content confocal imaging approach for Organs-on-Chips.* Lab on a Chip, 2019. **19**(3): p. 410-421.
51. Anari, P.Y., et al., *Automatic segmentation of clear cell renal cell tumors, kidney, and cysts in patients with von Hippel-Lindau syndrome using U-net architecture on magnetic resonance images.* ArXiv, 2023.
52. Falk, T., et al., *U-Net: deep learning for cell counting, detection, and morphometry.* Nat Methods, 2019. **16**(1): p. 67-70.
53. Jeong, E.J., D. Choi, and D.W. Lee, *U-Net Deep-Learning-Based 3D Cell Counter for the Quality Control of 3D Cell-Based Assays through Seed Cell Measurement.* SLAS Technol, 2021. **26**(5): p. 468-476.
54. Zhu, N., et al., *Segmentation with Residual Attention U-Net and an Edge-Enhancement Approach Preserves Cell Shape Features.* Annu Int Conf IEEE Eng Med Biol Soc, 2022. **2022**: p. 2115-2118.
55. Grys, B.T., et al., *Machine learning and computer vision approaches for phenotypic profiling.* J Cell Biol, 2017. **216**(1): p. 65-71.
56. Tek, F.B., A.G. Dempster, and I. Kale, *Computer vision for microscopy diagnosis of malaria.* Malar J, 2009. **8**: p. 153.
57. Wu, K., D. Gauthier, and M.D. Levine, *Live cell image segmentation.* IEEE Trans Biomed Eng, 1995. **42**(1): p. 1-12.
58. Din, N.U. and J. Yu, *Training a deep learning model for single-cell segmentation without manual annotation.* Sci Rep, 2021. **11**(1): p. 23995.
59. Badrinarayanan, V., A. Kendall, and R. Cipolla, *SegNet: A Deep Convolutional Encoder-Decoder Architecture for Image Segmentation.* Ieee Transactions on Pattern Analysis and Machine Intelligence, 2017. **39**(12): p. 2481-2495.
60. Rivenson, Y., et al., *Virtual histological staining of unlabelled tissue-autofluorescence images via deep learning.* Nat Biomed Eng, 2019. **3**(6): p. 466-477.
61. Baghba, R., et al., *Tumor microenvironment complexity and therapeutic implications at a glance.* Cell Communication and Signaling, 2020. **18**(1).
62. Whiteside, T.L., *The tumor microenvironment and its role in promoting tumor growth.* Oncogene, 2008. **27**(45): p. 5904-5912.
63. Bejarano, L., M.J.C. Jordao, and J.A. Joyce, *Therapeutic Targeting of the Tumor Microenvironment.* Cancer Discovery, 2021. **11**(4): p. 933-959.
64. Shintani, Y., et al., *Therapeutic Targeting of Cancer-Associated Fibroblasts in the Non-Small Cell Lung Cancer Tumor Microenvironment.* Cancers, 2023. **15**(2).
65. Chung, M., et al., *Biomimetic Model of Tumor Microenvironment on Microfluidic Platform.* Advanced Healthcare Materials, 2017. **6**(15).
66. Bahcecioglu, G., et al., *Breast cancer models: Engineering the tumor microenvironment.* Acta Biomaterialia, 2020. **106**: p. 1-21.

67. Tomas-Bort, E., et al., *3D approaches to model the tumor microenvironment of pancreatic cancer.* Theranostics, 2020. **10**(11): p. 5074-5089.
68. Ko, J., et al., *Tumor spheroid-on-a-chip: a standardized microfluidic culture platform for investigating tumor angiogenesis.* Lab Chip, 2019. **19**(17): p. 2822-2833.
69. Esch, E.W., A. Bahinski, and D. Huh, *Organs-on-chips at the frontiers of drug discovery.* Nature Reviews Drug Discovery, 2015. **14**(4): p. 248-260.
70. Sontheimer-Phelps, A., B.A. Hassell, and D.E. Ingber, *Modelling cancer in microfluidic human organs-on-chips.* Nature Reviews Cancer, 2019. **19**(2): p. 65-81.
71. Subia, B., et al., *Breast tumor-on-chip models: From disease modeling to personalized drug screening.* Journal of Controlled Release, 2021. **331**: p. 103-120.
72. Mansour, A.A., et al., *An in vivo model of functional and vascularized human brain organoids (vol 36, pg 432, 2018).* Nature Biotechnology, 2018. **36**(8): p. 772-772.
73. Grebenyuk, S. and A. Ranga, *Engineering Organoid Vascularization.* Frontiers in Bioengineering and Biotechnology, 2019. **7**.
74. Pham, M.T., et al., *Generation of human vascularized brain organoids.* Neuroreport, 2018. **29**(7): p. 588-593.
75. Lee, Y., et al., *Microfluidics within a well: an injection-molded plastic array 3D culture platform.* Lab on a Chip, 2018. **18**(16): p. 2433-2440.
76. Lim, J., et al., *Microvascularized tumor organoids-on-chips: advancing preclinical drug screening with pathophysiological relevance.* Nano Converg, 2021. **8**(1): p. 12.
77. Pandya, H.J., et al., *A microfluidic platform for drug screening in a 3D cancer microenvironment.* Biosensors and Bioelectronics, 2017. **94**: p. 632-642.
78. Demello, A.J., *Control and detection of chemical reactions in microfluidic systems.* Nature, 2006. **442**(7101): p. 394-402.
79. Eduati, F., et al., *A microfluidics platform for combinatorial drug screening on cancer biopsies.* Nature communications, 2018. **9**(1): p. 2434.
80. Yue, T., et al., *A modular microfluidic system based on a multilayered configuration to generate large-scale perfusable microvascular networks.* Microsystems & nanoengineering, 2021. **7**(1): p. 4.
81. Chung, M., et al., *Wet-AMD on a Chip: Modeling Outer Blood-Retinal Barrier In Vitro.* Advanced Healthcare Materials, 2018. **7**(2).
82. Jalili-Firoozinezhad, S., et al., *A complex human gut microbiome cultured in an anaerobic intestine-on-a-chip (vol 3, pg 583, 2019).* Nature Biomedical Engineering, 2019. **3**(7): p. 583-583.
83. Pocock, K., et al., *Uptake of silica particulate drug carriers in an intestine-on-a-chip: towards a better in vitro model of*

nanoparticulate carrier and mucus interactions. Biomaterials Science, 2019. **7**(6): p. 2410-2420.
84. Lee, Y., et al., *Microfluidics within a well: an injection-molded plastic array 3D culture platform.* Lab on a Chip, 2018. **18**(16): p. 2433-2440.
85. Vulto, P., et al., *Phaseguides: a paradigm shift in microfluidic priming and emptying.* Lab on a Chip, 2011. **11**(9): p. 1596-1602.
86. Berthier, E., E.W.K. Young, and D. Beebe, *Engineers are from PDMS-land, Biologists are from Polystyrenia.* Lab on a Chip, 2012. **12**(7): p. 1224-1237.
87. Ko, J., et al., *Human Ocular Angiogenesis-Inspired Vascular Models on an Injection-Molded Microfluidic Chip.* Advanced Healthcare Materials, 2019. **8**(15).
88. Trietsch, B., et al., *Membrane-Free Culture and Real-Time Barrier Integrity Assessment of Perfused Intestinal Epithelium Tubes.* Drug Metabolism and Pharmacokinetics, 2018. **33**(1): p. S45-S46.
89. Yu, J., et al., *Perfusable micro-vascularized 3D tissue array for high-throughput vascular phenotypic screening.* Nano Convergence, 2022. **9**(1).
90. Mencattini, A., et al., *From Petri Dishes to Organ on Chip Platform: The Increasing Importance of Machine Learning and Image Analysis.* Frontiers in Pharmacology, 2019. **10**.
91. Urban, G., et al., *Deep Learning for Drug Discovery and Cancer Research: Automated Analysis of Vascularization Images.* Ieee-Acm Transactions on Computational Biology and Bioinformatics, 2019. **16**(3): p. 1029-1035.
92. Riordon, J., et al., *Deep Learning with Microfluidics for Biotechnology*. Trends in Biotechnology, 2019. **37**(3): p. 310-324.
93. Goodfellow, I.J., et al., *Generative Adversarial Nets.* Advances in Neural Information Processing Systems 27 (Nips 2014), 2014. **27**: p. 2672-2680.
94. Isola, P., et al., *Image-to-Image Translation with Conditional Adversarial Networks.* 30th Ieee Conference on Computer Vision and Pattern Recognition (Cvpr 2017), 2017: p. 5967-5976.
95. Weigert, M., et al., *Content-aware image restoration: pushing the limits of fluorescence microscopy.* Nature Methods, 2018. **15**(12): p. 1090-+.
96. Ouyang, W., et al., *Deep learning massively accelerates super-resolution localization microscopy.* Nature Biotechnology, 2018. **36**(5): p. 460-+.
97. Mittal, M., et al., *Deep learning based enhanced tumor segmentation approach for MR brain images.* Applied Soft Computing, 2019. **78**: p. 346-354.
98. Rivenson, Y., et al., *Virtual histological staining of unlabelled tissue-autofluorescence images via deep learning.* Nature Biomedical Engineering, 2019. **3**(6): p. 466-477.

99. Rivenson, Y., et al., *PhaseStain: the digital staining of label-free quantitative phase microscopy images using deep learning.* Light-Science & Applications, 2019. **8**.
100. Ben-Yehuda, K., et al., *Simultaneous Morphology, Motility, and Fragmentation Analysis of Live Individual Sperm Cells for Male Fertility Evaluation.* Advanced Intelligent Systems, 2022. **4**(4).
101. Christiansen, E.M., et al., *In Silico Labeling: Predicting Fluorescent Labels in Unlabeled Images.* Cell, 2018. **173**(3): p. 792-+.
102. Chen, Z.Z., et al., *Automated evaluation of tumor spheroid behavior in 3D culture using deep learning-based recognition.* Biomaterials, 2021. **272**.
103. Anagnostidis, V., et al., *Deep learning guided image-based droplet sorting for on-demand selection and analysis of single cells and 3D cell cultures.* Lab on a Chip, 2020. **20**(5): p. 889-900.
104. Tran, T., et al., *Blood Cell Images Segmentation using Deep Learning Semantic Segmentation.* 2018 Ieee International Conference on Electronics and Communication Engineering (Icece 2018), 2018: p. 13-16.
105. Isozaki, A., et al., *AI on a chip.* Lab on a Chip, 2020. **20**(17): p. 3074-3090.
106. Lee, S., et al., *Modeling 3D Human Tumor Lymphatic Vessel Network Using High-Throughput Platform.* Advanced Biology, 2021. **5**(2).
107. Zhang, T.Y. and C.Y. Suen, *A Fast Parallel Algorithm for Thinning Digital Patterns.* Communications of the Acm, 1984. **27**(3): p. 236-239.
108. Ronneberger, O., P. Fischer, and T. Brox, *U-Net: Convolutional Networks for Biomedical Image Segmentation.* Medical Image Computing and Computer-Assisted Intervention, Pt Iii, 2015. **9351**: p. 234-241.
109. Simonyan, K. and A. Zisserman, *Very deep convolutional networks for large-scale image recognition.* arXiv preprint arXiv:1409.1556, 2014.
110. Chen, J., et al., *Three-dimensional residual channel attention networks denoise and sharpen fluorescence microscopy image volumes.* Nature methods, 2021. **18**(6): p. 678-687.
111. Schmauch, B., et al., *A deep learning model to predict RNA-Seq expression of tumours from whole slide images.* Nature communications, 2020. **11**(1): p. 3877.
112. Metzger, J.J., et al., *Deep-learning analysis of micropattern-based organoids enables high-throughput drug screening of Huntington's disease models.* Cell Reports Methods, 2022. **2**(9).
113. Fan, K., et al., *A machine learning assisted, label-free, non-invasive approach for somatic reprogramming in induced pluripotent stem cell colony formation detection and prediction.* Scientific reports, 2017. **7**(1): p. 13496.

114. Popovic, N., S. Vujosevic, and T. Popovic, *Regional Patterns in Retinal Microvascular Network Geometry in Health and Disease.* Scientific Reports, 2019. **9**.
115. Zaitoun, I.S., et al., *Bcl-2 Expression in Pericytes and Astrocytes Impacts Vascular Development and Homeostasis.* Scientific Reports, 2019. **9**.

Abstract in Korean

장기칩(Organ-on-a-chio)은 고도로 생체 환경을 모사하여 복잡한 생체 환경을 작은 미세유체(microfluidic) 플랫폼에 구현하는 체외 모델이다. 미세유체 기술의 발전으로 모세관류(Capillary flow)를 활용한 다양한 역학적 해석(Concus-Finn condition, Spontaneous Capillary Flow condition 등)을 통하여 미세 채널에 소량의 유체를 정밀하게 조작하고 제어하여 복잡한 세포 미세환경 구현이 가능하여 장기칩은 더욱 정교해지고 기존에서 구현하지 못했던 복잡한 체내 구조나 다양한 배양 환경 구현이 가능하다. 특히 실제 종양 미세환경(Tumor microenvironment)를 구현하기 위하여 혈관화된 종양(Vascularized spheroid) 혹은 오가노이드(Vascularized organoid) 모델에 대한 연구의 중요성은 점점 커지고 있다. 혈관화된 모델은 복잡한 체내와 유사한 환경을 제공하여 다양한 약물에 대한 독성 시험, 유동 순환 시스템 연구에 활용되어 한 단계 더 진보된 결과를 기대할 수 있다. 혈관화된 모델에서는 배양 조직, 종양 또는 혈관의 형태(morphology), 기관 생리학(organ physiology), 약물 반응 등에 대한 중요한 정보를 얻을 수 있으며 이러한 데이터들을 추적하여 다양한 결과를 도출할 수 있다.

그러나 이러한 플랫폼은 두 가지 한계점을 지니고 있다. 첫째, 지금까지의 종양 미세환경 플랫폼은 소규모 종양 ($\sim 400\mu m$) 의 공배양하여 다양한 약물 스크리닝과 연구가 진행되었다. 허나 실제 체내의 환경은 이보다 훨씬 대규모 스케일의 실제 조직이나 오가노이드($1000\mu m \sim 2000\mu m$)가 자라며 이를 실제로 구현할 수 있는 새로운 플랫폼 연구의 필요성이 대두된다. 둘째, 장기칩 분야는 지속적으로 발전하여 실험 수율과 효율이 증가하기에 많은 양의 실험 데이터를 생산할 수 있는 조건이 갖춰졌다. 하지만 장기칩은 3D 종양 미세환경을 구현하였기에 공초점 현미경(Confocal microscopy)을 활용하여 이미징 데이터를 생산한다. 공초점 현미경은 높은 퀄리티의 이미징을 제공해주지만 비용이 비싸며 이미징 시간이 길다는 단점으로 모든 데이터를 처리할 때 병목 현상이 발생한다.

한계점을 극복하기 위해 두 가지 해결책을 제안한다. 첫째, 기존의 장기칩에서 활용하는 레일 구조(Rail guided structure)와 메쉬 구조(Mesh-assisted structure)를 결합하여 대규모 스케일의 혈관화된 조직이나 오가노이드를 배양할 수 있는 새로운 플랫폼인 Vascularized Tissue-Micromesh Assisted Platform (VT-MAP)을 소개합니다. VT-MAP 은 소규모 종양 모델을 벗어나 단순히 대규모 종양을 손쉽게 배양할 수 있을뿐만 아니라 혈관화된 종양 모델을 제공하여 혈관을 통한 약물 전달 모델을 제공할 수 있다. 이를 통해 VT-MAP 은 기존의 체외모델의 한계를 극복하고 새로운 약물 개발과 정밀의학 연구에

새로운 가능성을 줄 것으로 기대한다. 둘째, 기존의 공초점 현미경 이미징 시스템을 벗어나 신속한 처리가 가능한 비표지방식의 가상염색(Label-free virtual staining method) 기법인 Virtual Staining-assisted Injection Molded Plastic Array 3D Culture System (VS-IMPACT)을 소개한다. VS-IMACT 는 SegNet 과 cGAN 을 활용한 딥러닝 기반 알고리즘이며 혈관의 brightfield 이미지에서 바로 공초점 이미지(confocal image) 급의 형광 이미지를 별도의 처리 과정 없이 즉시 얻을 수 있다. 기존의 공초점 현미경 이미징 과정에서 반드시 필요한 면역세포화학 염색법(immunocytochemistry staining method)을 생략할 수 있으며 비표지방식의 실시간 세포 이미징 (label-free live cell imaging)이 가능하여 비파괴 및 실시간 혈관 모니터링이 가능하여 성장하는 양상을 손쉽게 확인하고 가상으로 염색된 데이터를 얻을 수 있다. 이 방식을 활용하면 종양 미세환경에서 혈관 생성 억제제나 항암제에 대한 반응을 평가할 수 있다.

본 논문에서 개발한 VT-MAP 과 VS-IMPACT 를 활용하면 종양 미세환경 연구의 한계점을 극복하고 새로운 연구 방식을 제시할 수 있을 것으로 기대한다.

주요어 : 장기칩, 혈관화된 조직, 미세유체역학, 대규모 스케일, 가상 염색, 딥러닝, 고효율 플랫폼

학번 : 2017-24396